Electrochimica Acta 548 (2026) 147858

Contents lists available at ScienceDirect

Electrochimica Acta

journal homepage: www.journals.elsevier.com/electrochimica-acta

Mixed Ni/Cu-sandwich dawson polyoxotungstates: Electrochemistry and DFT insights

Anaïs Abrousse [a,1], Ionut-Octavian Stan [b,1], Neus Vilà [c,d], Anne-Lucie Teillout [a], Khaoula Merimi [b], Coen de Graaf [b,e], Pedro de Oliveira [a], Xavier López [b,*], Israël Martyr Mbomekallé [a,*]

[a] Equipe d'Electrochimie et Photo-Electrochimie, Institut de Chimie Physique, UMR 8000 CNRS, Université Paris Saclay, Orsay F-91405, France
[b] Departament de Química Física i Inorgànica, Universitat Rovira i Virgili, Marcel·lí Domingo 1, 43007 Tarragona, Spain
[c] Université de Lorraine, CNRS, LCPME, F-54000 Nancy, France
[d] Departament de Química, Universitat Autonoma de Barcelona, 08193 Bellaterra, Barcelona, Spain
[e] Institució Catalana de Recerca i Estudis Avançats (ICREA). Passeig Lluís Companys 23, 08010 Barcelona, Spain

ARTICLE INFO

Keywords:
Electrochemistry
DFT calculations
Polyoxometalates

ABSTRACT

Given the established electrocatalytic potential of Ni(II)- and Cu(II)-containing tungsten-based POMs, the primary objective of this work was to create a unique molecular architecture combining both active metal centres in the two Dawson sandwich POMs, $[(CuOH_2)_2Ni_2(As_2W_{15}O_{56})_2]^{16-}$ and $[(NiOH_2)_2Cu_2(As_2W_{15}O_{56})_2]^{16-}$. This aims to exploit potential synergistic effects for enhanced catalytic performance and to deepen the understanding of redox mechanisms in these mixed-metal systems. A detailed electrochemical study of the two POMs in solution, compared to their homometallic analogues containing only Ni(II) or only Cu(II) centres, was conducted using cyclic voltammetry (CV), also coupled to quartz crystal microbalance in order to monitor Cu deposition/desorption phenomena, and controlled potential coulometry, enabling unambiguous identification and differentiation. X-ray photoelectron spectroscopy (XPS) unequivocally corroborated these findings. Furthermore, density functional theory (DFT) calculations provide additional insights that are relevant to rationalise the electrochemical measurements. The molecular orbital sequence, energies and shapes provide relevant supporting information to the experimental facts. Combined evidence establishes that Na/Ni compounds maintain the W-only electrochemical fingerprint, whereas new CV features appear when Cu(II) is part of the structure, modulated by the rest of the equatorial composition. Protonation has been explored and its effects on the redox chemistry examined at the theoretical level.

1. Introduction

Polyoxometalates (POMs) constitute a class of discrete molecular entities whose physicochemical properties can be finely tuned. Often considered as soluble analogues of molecular oxides, these species exhibit considerable potential due to the variability in their size, structure, and chemical composition [1–10] The development of multi-step stereoselective synthesis strategies allows for the rational incorporation of various metallic cations, thereby generating POM architectures that prove to be privileged nano-objects for the investigation of reaction mechanisms, particularly in electrochemistry [11–25] Our interest has focused, over the past few years, on heterometallic sandwich-type POMs derived from the Dawson structure, characterised by a central metallic cluster composed of metal centres of distinct nature [26–31]

In this study, our attention was directed towards two POMs, $[(CuOH_2)_2Ni_2(As_2W_{15}O_{56})_2]^{16-}$ and $[(NiOH_2)_2Cu_2(As_2W_{15}O_{56})_2]^{16-}$ (abbreviated **$[(H_2O\text{-}Cu)_2\text{-}Ni_2]$** and **$[(H_2O\text{-}Ni)_2\text{-}Cu_2]$** in the following, respectively), sharing a common structure formed by two $[As_2W_{15}O_{56}]^{12-}$ Dawson fragments that sandwich a metallic cluster in the equatorial region, comprising two copper and two nickel ions (see Fig. 1). These POMs exhibit an identical chemical composition and nearly identical crystallographic structure, differing solely in the relative arrangement of the Cu(II) and Ni(II) centres within the cluster. In **$[(H_2O\text{-}Cu)_2\text{-}Ni_2]$**, the Ni(II) centres occupy internal positions in the

---

* Corresponding authors.
E-mail addresses: javier.lopez@urv.cat (X. López), israel.mbomekalle@universite-paris-saclay.fr (I.M. Mbomekallé).
[1] Have equally contributed

https://doi.org/10.1016/j.electacta.2025.147858
Received 11 November 2025; Accepted 20 November 2025

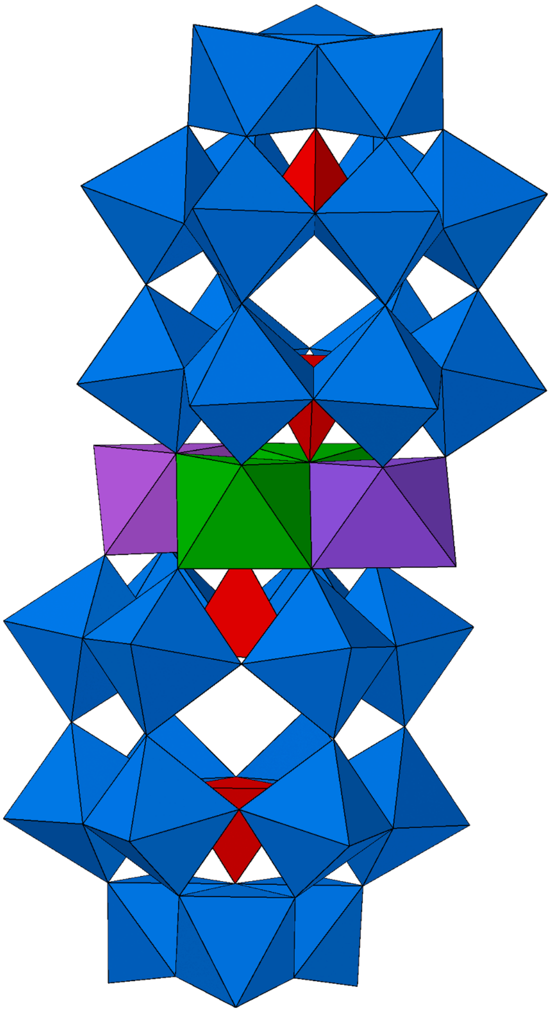

Fig. 1. Polyhedral representation of the mixed-sandwich POM structure $[(MOH_2)_2M'_2(As_2W_{15}O_{56})_2]^{16-}$. Blue octahedra represent WO_6 groups, whereas green and purple octahedra represent MO_6 and $M'O_6$ (for Ni or Cu) blocks. The red tetrahedra are AsO_4 groups.

equatorial metallic cluster, adopting an octahedral environment where each is coordinated to six oxygen atoms which, in turn, are each bonded to a tungsten atom belonging to the $[As_2W_{15}O_{56}]^{12-}$ fragments. Conversely, the Cu(II) centres are located in external positions of the central cluster, within a distinct octahedral environment consisting of five oxygen atoms from the tungstic framework and a sixth oxygen atom belonging to an aqua group. **$[(H_2O\text{-}Ni)_2\text{-}Cu_2]$** displays the reverse configuration in the metallic cluster, with the Cu(II) centres in the internal positions and the Ni(II) centres in the external positions.

The significant potential of tungsten-based POMs containing Ni(II) or Cu(II) metal centres in various electrocatalytic processes has been revealed, notably in the reduction of nitrogen oxides, dioxygen and hydrogen peroxide, emphasizing their catalytic versatility [31–48] Within the scope of the fundamental research preceding these possible applications, this study aims to provide a comprehensive electrochemical characterisation of the redox behaviour of the two newly synthesised mixed-sandwich POMs, comprising two Cu(II) and two Ni(II) centres within their equatorial metal cluster. By direct comparison with the corresponding Cu(II)-only and Ni(II)-only analogues, this work seeks to elucidate the fundamental charge-transfer mechanisms — involving both electrons and protons — with further insight provided by DFT calculations.

We conducted a detailed electrochemical study of the two POMs in solution, comparing them to their homometallic analogues containing two, or four Ni(II) or Cu(II) centres (see Table S1). The combined use of various electrochemical techniques, including cyclic voltammetry, coupled to the quartz crystal microbalance, as well as controlled potential coulometry, enabled an unambiguous identification of each POM and the differentiation from its analogues. Furthermore, the results obtained by XPS spectroscopy unequivocally corroborated the observations and conclusions derived from the electrochemical study. Theoretical calculations based on density functional theory (DFT) allowed us to better interpret the experiments. Based on the results obtained from the study of the redox behaviour of these POMs and the theoretical calculations, we were able to anticipate and explore certain electrocatalytic properties of these different compounds.

2. Experimental section

2.1. *Chemicals and reagents*

Pure water obtained with a Milli-Q Integral 5 purification set was used throughout. All reagents were of high-purity grade and were used as purchased without further purification. Sodium tungstate dihydrate ($Na_2WO_4{\cdot}2H_2O$, 99 %, Sigma-Aldrich), hydrochloric acid (HCl, 36.5–38 % Riedel de Haen), sulfuric acid (H_2SO_4, 98 %, Sigma-Aldrich), acetic acid (CH_3COOH, 100 %, Prolabo), lithium acetate dihydrate ($LiCH_3COO{\cdot}2H_2O$, Sigma Aldrich), nickel nitrate hexahydrate ($Ni(NO_3)_2{\cdot}6H_2O$, Prolabo), copper sulfate pentahydrate ($CuSO_4{\cdot}5H_2O$, Prolabo), sodium chloride (NaCl, Acros Organics), and lithium sulfate monohydrate ($Li_2SO_4.H_2O$, Prolabo).

$[As_2W_{15}O_{56}]^{12-}$ (**As_2W_{15}**), $[(NaOH_2)_2Cu_2(As_2W_{15}O_{56})_2]^{18-}$ (**$[(H_2O\text{-}Na)_2\text{-}Cu_2]$**), $[(CuOH_2)_2Cu_2(As_2W_{15}O_{56})_2]^{16-}$ (**$[(H_2O\text{-}Cu)_2\text{-}Cu_2]$**), $[(NaOH_2)_2Ni_2(As_2W_{15}O_{56})_2]^{18-}$ (**$[(H_2O\text{-}Na)_2\text{-}Ni_2]$**) and $[(NiOH_2)_2Ni_2(As_2W_{15}O_{56})_2]^{16-}$ (**$[(H_2O\text{-}Ni)_2\text{-}Ni_2]$**) were prepared by the following synthetic procedures previously reported [49–52]. The synthesis of $[(CuOH_2)_2Ni_2(As_2W_{15}O_{56})_2]^{16-}$ (**$[(H_2O\text{-}Cu)_2\text{-}Ni_2]$**) and $[(NiOH_2)_2Cu_2(As_2W_{15}O_{56})_2]^{16-}$ (**$[(H_2O\text{-}Ni)_2\text{-}Cu_2]$**) was adapted from the method used for compounds containing two metal centres [26–28,30, 31] Table S1 in the ESI presents the chemical formulas and abbreviated notations of all the POMs used in this study. Expected corresponding structures are presented on Scheme 1 below.

2.2. *XPS analysis*

XPS analysis of the six polyoxotungstates, **$[(H_2O\text{-}Na)_2\text{-}Ni_2]$**, **$[(H_2O\text{-}Ni)_2\text{-}Ni_2]$**, **$[(H_2O\text{-}Na)_2\text{-}Cu_2]$**, **$[(H_2O\text{-}Cu)_2\text{-}Cu_2]$**, **$[(H_2O\text{-}Cu)_2\text{-}Ni_2]$**, **$[(H_2O\text{-}Ni)_2\text{-}Cu_2]$** was performed in order to quantify the composition of the powders.

XPS measurements were recorded on a Kratos Axis Ultra X-Ray photoelectron spectrometer equipped with a microfocused (300 × 700 μm^2) monochromatic radiation (Al Kα source, 1486.6 eV) operating at 120 W under a residual pressure of about 10^{-9} mbar. The spectra were collected at a take-off angle of 90° with a pass energy of 20 eV. Charge compensation was applied by flooding low-energy electrons. All spectra were energy-calibrated assigning the adventitious carbon C 1s a binding energy of 285.0 eV. Spectra were mathematically fitted with Casa XPS software using a least-squares algorithm and a nonlinear Shirley-type background. The fitting peaks of the experimental curves were defined by a combination of Gaussian (70 %) and Lorentzian (30 %) distributions. The core level spectra were used to evaluate the atomic concentration of the species present in the powders. The atomic concentrations were estimated from the relative peak areas of the spectrum and the corresponding sensitivity factors according to Eq. (1):

$$At.\% = \frac{\left(\frac{A_i}{S_i}\right)}{\sum\left(\frac{A_i}{S_i}\right)} \tag{1}$$

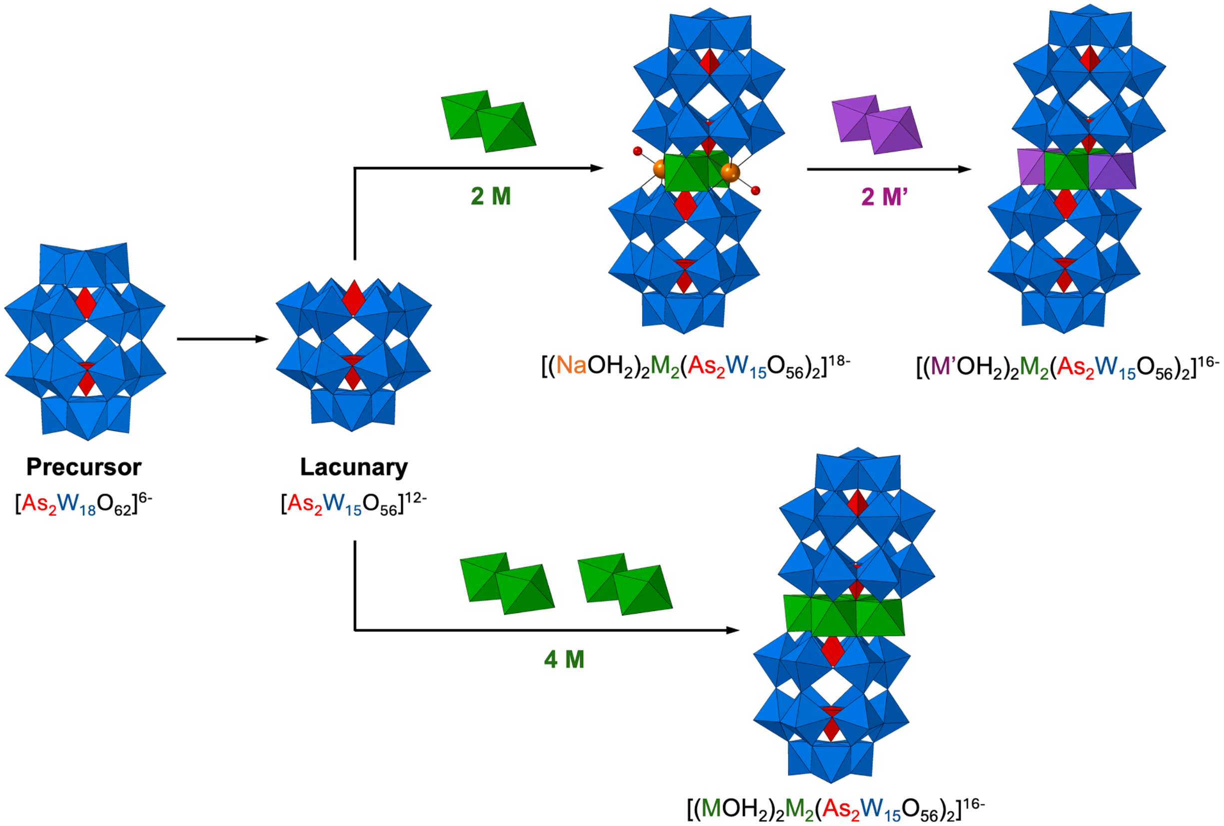

Scheme 1. Synthetic steps for the formation of mixed (top branch) and single-metal sandwich POMs (bottom branch) from the Wells-Dawson $[As_2W_{18}O_{62}]^{6-}$ precursor.

where A_i is the peak area of the element I and S_i is the sensitivity factor for this element. Sensitivity factor values of 1, 2.93, 4.07, 16.33, 22.18 and 25.39, were used for C 1s, O 1s, As 3p, W 4d, Ni 2p and Cu 2p, respectively.

2.3. Electrochemical experiments

Electrochemical data were obtained using an EG & G 273 A driven by a PC with the M270 software. A one-compartment cell with a standard three-electrode configuration was used for cyclic voltammetry experiments. The reference electrode was a saturated calomel electrode (SCE), the counter electrode a platinum gauze of large surface area; both electrodes separated from the bulk electrolyte solution via fritted compartments filled with the same electrolyte. The working electrode was a 3 mm OD edge-plane pyrolytic graphite disc (EPG, Mersen, France). The pre-treatment of this electrode before each experiment, adapted from the procedure described in a former work [53], was as follows: 1. Fine polishing using diamond pastes (DP Diamond-Struers) of decreasing grain size (3 min with a grain size of 6 µm, 3 min with a grain size of 3 µm and 6 min with a grain size of 1 µm). The electrode then underwent two successive ultrasonic washings in ethanol and in Millipore water, respectively, lasting for 5 min each. Results were highly reproducible from one experiment to another and slight variations observed over successive runs are rather attributed to the uncertainty associated with the detection limit of our equipment (potentiostat, hardware and software) rather than to working electrode pre-treatment or possible variations in temperature.

The composition of the various media was as follows: 0.2 M Li_2SO_4 + H_2SO_4 for pH 2.0 and 0.4 M CH_3COOLi + CH_3COOH for pH 4.0. The polyanion concentration was 2×10^{-4} M. Prior to each experiment, solutions were de-aerated thoroughly for at least 30 min with pure Ar. A positive pressure of this gas was maintained during subsequent work. Cyclic voltammograms were recorded at different scan rates according to the purpose of the experiments. All experiments were performed at room temperature, which was close to 20 °C in our laboratory.

2.4. Electrochemical quartz crystal microbalance (EQCM)

The electrochemical quartz crystal microbalance (EQCM) setup used in this work was the model QCA 922 (Seiko/EG&G) with 9 MHz AT-cut crystals. New crystals equipped with carbon electrodes provided by Seiko were employed, since classical gold or platinum electrodes were inappropriate for the present study. The geometric surface area of these carbon electrodes was 0.20 cm^2.

2.5. Computational details

To model the structural and electronic features of the studied systems, density functional theory (DFT) calculations were performed with Gaussian16[54] and ADF2022[55] programs. The unrestricted spin formalism was applied assuming high-spin open-shell electronic configurations for the transition metal centers (Ni and Cu), a scenario that aligns with experimental observations and prior theoretical studies.

Geometry optimisations were carried out using ADF2022 for its superior use of molecular symmetry, with the BP86 functional[56] and the triple-ζ with polarization (TZP) basis sets for all atoms along with scalar relativistic effects via the Zeroth Order Regular Approximation (ZORA) [57] The effects of the surrounding solvent (water, $\varepsilon = 78.4$) were introduced with the Conductor-like Screening Model (COSMO) [58] With the optimised molecular geometries, we performed single point calculations using Gaussian16 to obtain molecular orbital energies, total molecular electronic energies and spin densities. In this step, the B3LYP functional[59,60] was employed because of its proven reliability in reproducing electronic properties over a broad range of systems. O atoms not bonded to Cu and Ni were described with an all-electron double-ζ + polarization 6–31G(d,p) basis set. W and As atoms (not located in the equatorial region) were treated with valence double-ζ LANL2DZ basis sets, which incorporate ECPs for the core electrons. The atoms in the equatorial region were described with more extended basis sets for a more accurate description of the electronic behaviour critical for redox processes: for H and O in aqua groups, and O and Na atoms directly bonded to the sandwiched metal centers, we used all-electron triple-ζ + polarization 6–311G(d,p) basis sets. Similarly, for transition metals (Ni and Cu) we employed valence triple-ζ + polarization LANL2TZ(f) basis sets with the corresponding effective core potentials (ECPs). Solvent effects in Gaussian calculations were modeled using the Polarizable Continuum Model (PCM)[61] with water as the solvent. Additionally, Grimme's dispersion corrections[62] (GD3BJ) were applied in all single point calculations to account for long-range dispersion effects.

3. Results and discussion

3.1. XPS analysis

Representative XPS survey spectra recorded for the six compounds were performed in order to quantify the composition of the powders (Figure S1). The Cu 2p, Ni 2p, As 3p, Na 1s and W 4d are observed at 934, 855, 145, 1071 and 247 eV, respectively, in addition to the C 1s (285 eV) and the O 1s (530 eV) peaks. Table 1 presents the elemental composition of the six compounds analysed via XPS in this study, as previously noted. Sodium ions (Na^+) were excluded from the elemental composition calculations. The determined elemental composition is in excellent agreement with the expected stoichiometry of the molecules.

It is important to highlight that the amount of W, As and O in each compound remains nearly constant (see Table 1) in agreement with the stoichiometry of the analysed molecules, as can be observed in Figures S2-S4 corresponding to the high-resolution spectra of W 4d, As 3p and O 1s, respectively. It should be noted that although the W 4f signal is typically used to study tungsten by XPS since it is easier to excite by X-Ray sources, here the W 4d core level was considered for the quantification due to the overlapping of the W 4f and the As 3d signals. The experimental data presented in Table 1 align well with the expected powder composition based on the molecular formula. In this sense, Figure S2 displays the W 4d core level spectra recorded for the six compounds. The main envelope of the W 4d core level spectra was curve-fitted, in all the cases, with a single doublet, exhibiting binding energies of 247.7 and 260.2 eV for the W $4d_{5/2}$ and the W $4d_{3/2}$ lines, respectively. This doublet, characterised by a spin-orbit splitting of 12.5 eV, is indicative of the presence of W^{6+} ions. Figure S3 shows the As 3p core level spectra for the six compounds. The main envelope of the As 3p core level spectra was curve-fitted, in all the cases, with a single doublet, exhibiting binding energies of 144.6 and 149.7 eV for the As $3p_{3/2}$ and the As $3p_{1/2}$ lines, respectively. The O 1s core level spectra were fitted with two components at 530.7 and 531.6 eV, in all the cases, which were attributed to the W-O and O-H bonds, respectively (Figure S4).

Table 1
Atomic composition of the powders estimated from the XPS data.

Compound	Atomic concentration / %					Atomic ratio		
	Cu	Ni	W	As	O	W/Cu	W/Ni	W/As
[$(H_2O\text{-}Na)_2$-Cu_2]	1.3	–	19.9	2.7	76.1	15.3 (15)	–	7.4 (7.5)
[$(H_2O\text{-}Cu)_2$-Cu_2]	2.6	–	19.7	2.6	75.1	7.6 (7.5)	–	7.6 (7.5)
[$(H_2O\text{-}Na)_2$-Ni_2]	–	1.3	20.0	2.6	76.1	–	15.3 (15)	7.6 (7.5)
[$(H_2O\text{-}Ni)_2$-Ni_2]	–	2.7	20.0	2.7	74.6	–	7.4 (7.5)	7.4 (7.5)
[$(H_2O\text{-}Cu)_2$-Ni_2]	1.3	1.3	19.8	2.6	75.0	15.2 (15)	15.2 (15)	7.6 (7.5)
[$(H_2O\text{-}Ni)_2$-Cu_2]	1.3	1.3	19.8	2.6	75.0	15.2 (15)	15.2 (15)	7.6 (7.5)

Theorical atomic ratio values are given in parentheses.

Fig. 2A displays the complex Cu 2p core-level spectrum, which for copper(II)-containing compounds shows its major component, Cu $2p_{3/2}$, centred around 934 eV. The XPS Cu $2p_{3/2}$ core-level spectra of the **[$(H_2O\text{-}Na)_2$-Cu_2]**, **[$(H_2O\text{-}Cu)_2$-Cu_2]**, **[$(H_2O\text{-}Cu)_2$-Ni_2]** and **[$(H_2O\text{-}Ni)_2$-Cu_2]** samples are presented in Fig. 2A (from top to bottom). The **[$(H_2O\text{-}Cu)_2$-Cu_2]** powder exhibits doublet peaks in the Cu $2p_{3/2}$ region, with components centred at 933.7 eV and 935.2 eV, respectively. Two hypotheses may explain the presence of these two components: (i) the coexistence of Cu(I) and Cu(II) species, with the lower binding energy component attributed to Cu(I) and the peak at 934.9 eV to Cu(II); or (ii) the presence of two distinct Cu $2p_{3/2}$ components arising from non-equivalent Cu^{2+} centres located at internal and external positions within the sandwich-type POM structure. The first hypothesis was discarded, since Cu(I) formation in this context would originate from X-ray-induced reduction of Cu(II), which should lead to time-dependent spectral changes, an effect that was not observed. Furthermore, considering the structural diversity of **[$(H_2O\text{-}Na)(H_2O\text{-}Cu)$-$Cu_2$]** and **[$(H_2O\text{-}Cu)_2$-$Cu_2$]**, the presence of two distinct Cu^{2+} species could be anticipated. The peak at 933.7 eV is attributed to external copper species, Cu-O-W-O, while the peak at 935.2 eV is associated with internal copper species, Cu-OH_2. As expected, given the stoichiometry of the molecule, the areas of these two components are approximately equal in the case of compound **[$(H_2O\text{-}Cu)_2$-Cu_2]**, whereas the relative area of the peak components of Cu $2p_{3/2}$ for compound **[$(H_2O\text{-}Na)(H_2O\text{-}Cu)$-$Cu_2$]** is 1:2. All the Cu 2p core level spectra exhibit broad satellite peaks located at 942.6 eV, a well-documented phenomenon for copper bonded to oxygen atoms that arise due to the interaction between the photoelectron and the surrounding oxygen atoms [63]

Analogous to the copper spectra, the Ni $2p_{3/2}$ spectra of nickel-containing compounds are shown in Fig. 2B **[$(H_2O\text{-}Ni)_2$-Ni_2]** powder exhibits doublet peaks in their Ni $2p_{3/2}$ spectra, with peaks at 855.3 and 856.2 eV (associated with non-equivalent Ni(II) sites). The peak at 855.3 eV is attributed to external Ni(II) sites (Ni-O-W-O), while the peak at 856.2 eV is associated with internal Ni(II) sites (Ni-OH_2).

3.2. Electrochemistry

Electrochemical characterisation was performed in 0.2 M Li_2SO_4 + H_2SO_4 / pH 2.0 and 0.4 M CH_3COOLi + CH_3COOH / pH 4.0 solutions. This is a comparative study of the redox properties of the different compounds using cyclic voltammetry (CV), controlled-potential coulometry (CPC), and electrochemical quartz crystal microbalance (EQCM).

3.2.1. *Comparative electrochemical study of As_2W_{15} vs [$(H_2O\text{-}Na)_2$-Ni_2] and [$(H_2O\text{-}Na)_2$-Cu_2]*

Initially, we aimed to compare the redox behaviour of sandwich-type compounds containing a bimetallic "d" cluster with the lacunary fragment **As_2W_{15}**, which acts as a ligand, in 0.2 M Li_2SO_4 + H_2SO_4 solution at pH 2.0. **As_2W_{15}** starts to decay after about 15 min in this medium. This degradation was progressive and continuous, leading to the appearance of new cathodic waves in the CV compared to the initial one, and a gradual decrease in the peak current of the original waves, confirming the instability of **As_2W_{15}** under these experimental conditions (Figure S5-A).

In 0.4 M CH_3COOLi + CH_3COOH solution at pH 4.0, the decay of **As_2W_{15}** was also manifested by a gradual decrease in the reduction peak currents (Figure S5-B).

All the waves observed in the CV of **As_2W_{15}** in both studied media are reversible electron transfer processes attributed to the W(VI) centres of the compound, the two As(V) centres remaining electrochemically silent in the explored potential range. When comparing the very first CVs

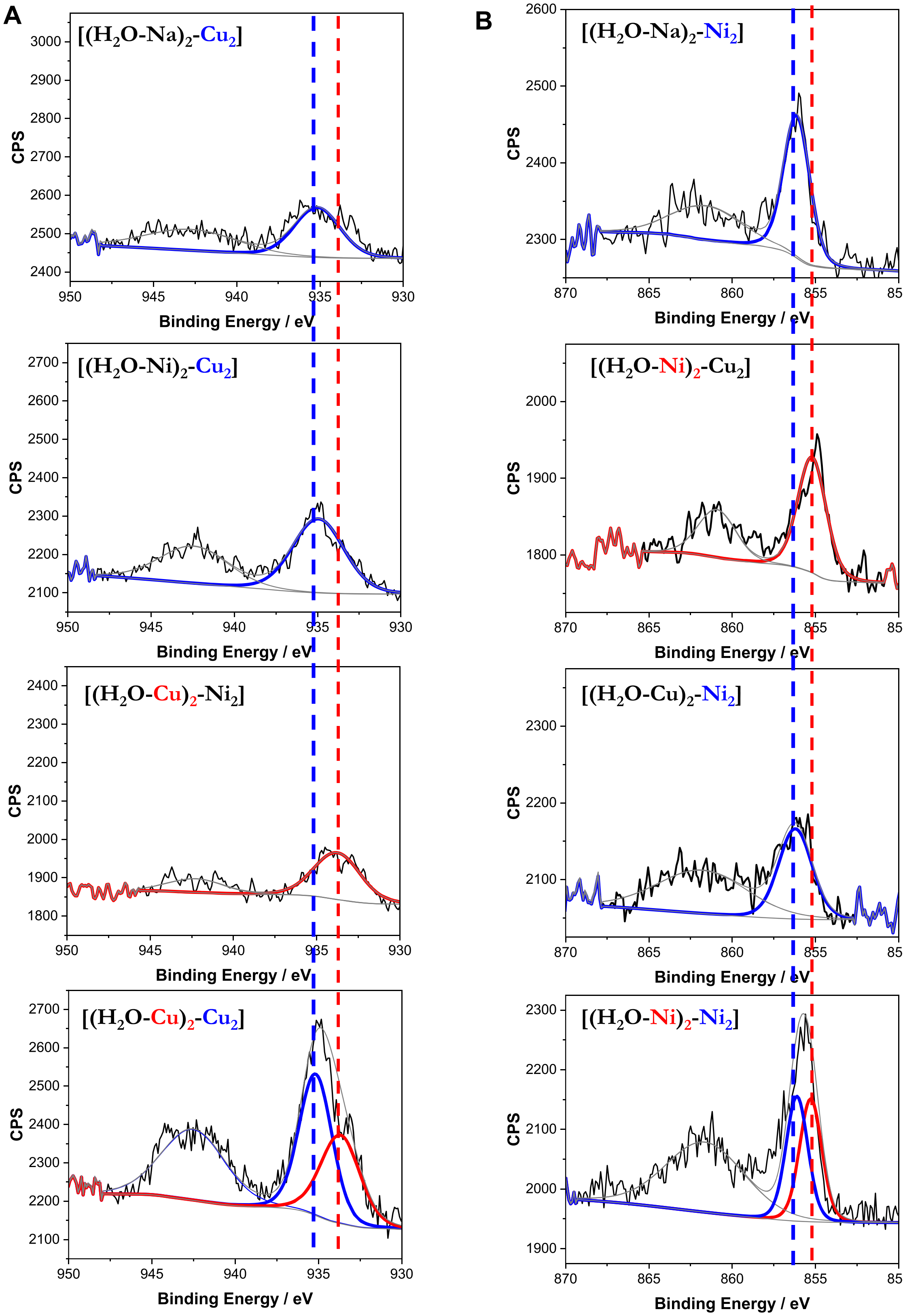

Fig. 2. (A) XPS Cu $2p_{3/2}$ core level spectra for compounds [$(H_2O\text{-}Na)_2\text{-}Cu_2$], [$(H_2O\text{-}Ni)_2\text{-}Cu_2$], [$(H_2O\text{-}Cu)_2\text{-}Ni_2$] and [$(H_2O\text{-}Cu)_2\text{-}Cu_2$]. (B) XPS Ni $2p_{3/2}$ core level spectra for compounds [$(H_2O\text{-}Na)_2\text{-}Ni_2$], [$(H_2O\text{-}Ni)_2\text{-}Cu_2$], [$(H_2O\text{-}Cu)_2\text{-}Ni_2$] and [$(H_2O\text{-}Ni)_2\text{-}Ni_2$].

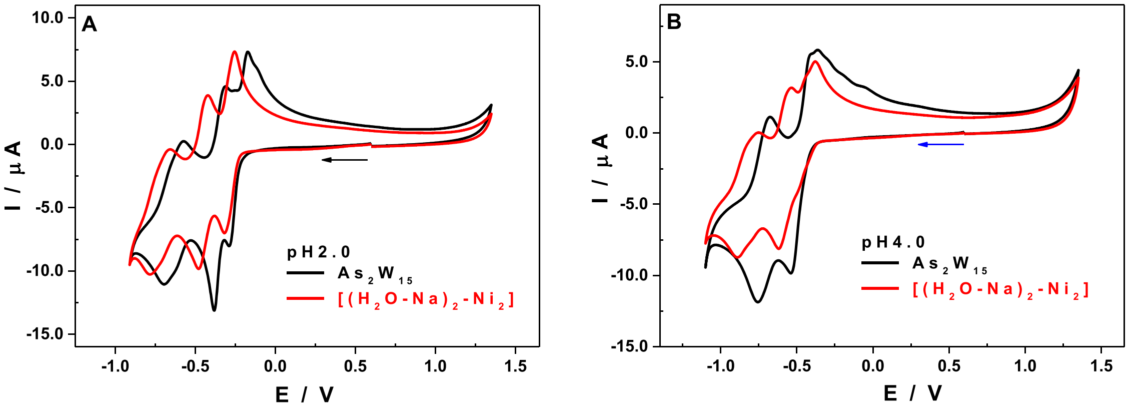

Fig. 3. CVs of $\mathbf{As_2W_{15}}$ (black) and $\mathbf{[(H_2O\text{-}Na)_2\text{-}Ni_2]}$ (red) recorded at a scan rate of 10 mV s^{-1} on a EPG electrode, in: (A) 0.2 M Li_2SO_4 + H_2SO_4 / pH 2.0; (B) 0.4 M CH_3COOLi + CH_3COOH / pH 4.0. Concentration of the bimetallic complexes: 0.2 mM. Concentration of $\mathbf{As_2W_{15}}$: 0.4 mM.

obtained for As_2W_{15} in both media (black line in Fig. 3A (pH 2) and Fig. 3B (pH 4)), a shift towards more negative potentials was observed for all cathodic redox waves attributed to the reduction of tungsten centres when going from pH 2.0 to pH 4.0, as expected. The first two bi-electronic reduction steps, which are well separated at pH 2.0 with two peaks at −0.30 V and −0.38 V vs. SCE, merged into a single four-electron step at pH 4.0, with the peak shifted to −0.57 V vs. SCE. The third cathodic system at pH 2.0, which became the second redox system at pH 4.0, was shifted by 60 mV towards more negative potentials (Figure S6 and Table 2).

When comparing the first CV of the $\mathbf{As_2W_{15}}$ with that of the complex containing two Ni(II) centres at pH 2.0, the first observation is a stabilising effect accompanying the formation of the $\mathbf{[(H_2O\text{-}Na)_2\text{-}Ni_2]}$ complex (Fig. 3A). Successive CVs of this complex are superimposable over a period exceeding 24 h. The stability of the $\mathbf{[(H_2O\text{-}Na)_2\text{-}Ni_2]}$ complex in this medium is confirmed by UV–visible spectroscopy results (See Figure S22). Indeed, like the CVs, the UV-visible spectra recorded for a solution of $\mathbf{[(H_2O\text{-}Na)_2\text{-}Ni_2]}$ at pH 2.0 are strictly overlayed over the same time interval. The rearrangement process, which very often leads to the conversion of the binuclear cluster complex to a trinuclear complex when the compound is in its synthesis medium, is not observed, at least not at the same rate [28] The stabilising effect is likely due to the presence of the Li^+ ion in the electrolyte, in contrast to the synthesis medium which contains the Na^+ ion. Nevertheless, it should be reminded that the pH of this study medium (pH 2.0) is considerably more acidic than that of the synthesis medium (pH 4.6).

In addition to the stabilising effect, a general shift of the voltammetric signals towards more negative potentials is observed at 10 mV s^{-1} when going from $\mathbf{As_2W_{15}}$ to $\mathbf{[(H_2O\text{-}Na)_2\text{-}Ni_2]}$ with cathodic potential peak shifts, ΔE_{pc}, ranging between 20 and 100 mV (see Table 2). The same observation is made at pH 4.0, namely $\mathbf{[(H_2O\text{-}Na)_2\text{-}Ni_2]}$ is more difficult to reduce than $\mathbf{As_2W_{15}}$, with the number and shape of the waves remaining globally identical (Fig. 3B).

Table 2
Peak potential (E_P) values (V vs. SCE) in 2 different media: pH 2.0 (0.2 M Li_2SO_4 + H_2SO_4) and pH 4.0 (0.4 M CH_3COOLi + CH_3COOH). POM concentration: 0.2 mM (0.4 mM for $\mathbf{As_2W_{15}}$).

pH 2.0					
		Cu_2	W_1	W_2	W_3
As_2W_{15}	E_{Pc}		−0.30	−0.38	−0.70
	E_{Pa}		−0.17	−0.31	−0.57
$[(H_2O\text{-}Na)_2Ni_2]$	E_{Pc}		−0.32	−0.48	−0.78
	E_{Pa}		−0.25	−0.42	−0.65
$[(H_2O\text{-}Na)_2Cu_2]$	E_{Pc}	−0.12	−0.28	−0.37	−0.62
	E_{Pa}	+0.01	−0.23	−0.31	−0.56
pH 4.0					
		Cu_2	W_1	W_2	W_3
As_2W_{15}	E_{Pc}		−0.57	−0.76	
	E_{Pa}		−0.35	−0.67	
$[(H_2O\text{-}Na)_2Ni_2]$	E_{Pc}		−0.50	−062	−0.89
	E_{Pa}		−0.38	−0.52	−0.75
$[(H_2O\text{-}Na)_2Cu_2]$	E_{Pc}	−0.35	−0.53	−0.75	
	E_{Pa}	+0.02	−0.36	−0.67	

These experimental results demonstrate that the sandwich-type complex, initially isolated in solid form, maintains its structural integrity in solution. Consequently, the existence of a dissociation equilibrium involving free Ni^{2+} cation and $[As_2W_{15}O_{56}]^{12-}$ is excluded.

The same stabilisation phenomenon of $\mathbf{As_2W_{15}}$ in pH 2.0 solution in the case of $\mathbf{[(H_2O\text{-}Na)_2\text{-}Ni_2]}$ is also observed with Cu(II) centres in the case of the $\mathbf{[(H_2O\text{-}Na)_2\text{-}Cu_2]}$ complex. The presence of copper leads to the appearance of new redox waves in the CV, attributable to the reduction of Cu(II) to Cu(0), which occurs at less negative potentials than those of the W(VI) centres (Fig. 4). The Cu(0) formed remains on the surface of the working electrode and, during the reverse scan, its re-oxidation (which occurs without diffusion from the bulk to the electrode surface) gives rise to a large, conical, and symmetric oxidation wave, characteristic of desorption phenomena. Its peak is located at around 0.01 V vs. SCE. The other reduction steps are attributable to the W(VI) centres. The third and last reduction step observable in this medium is followed by an irreversible step attributable to the electrocatalytic reduction of protons, that is the hydrogen evolution reaction (HER). Indeed, it becomes difficult to index a reduction potential peak on this wave, and the reduction current increases continuously while its reversibility disappears during the reverse scan (Fig. 4A). This phenomenon of catalytic H^+ ion reduction is related with a combination of three key factors: the relatively high H^+ concentration (pH 2.0), the accumulation of a significant number of electrons (exceeding 10 at this third step of reduction), and the modification of the working electrode surface by Cu(0) deposition. Under identical experimental conditions, the POM containing only two Ni(II) centres does not exhibit the same catalytic effect, as previously described. However, in a more acidic environment (pH 0.3) and following deposition onto an electrode surface, this same structure incorporating Ni(II) centres shows notable efficiency in the catalysis of the HER [46]

A similar electrochemical behaviour is observed at pH 4.0 with a shift of the potentials towards more negative values, compared to the values obtained at pH 2.0 (Fig. 4B). The same comparisons were conducted at a scan rate of 10 mV s^{-1} (Figure S7). The CVs recorded at higher scan rates (Figures S8 and S9) present similar features, indicating that the electrochemical processes involved are essentially the same, independent of the kinetics imposed by the scan rate.

Similarly to the $\mathbf{[(H_2O\text{-}Na)_2\text{-}Ni_2]}$ complex, the obtained results demonstrate that the $\mathbf{[(H_2O\text{-}Na)_2\text{-}Cu_2]}$ complex also exhibits remarkable stability in solution in both media under study. Furthermore, the data suggest that during the reduction process, Cu(II) centres are decoordinated from the POM framework and are deposited onto the

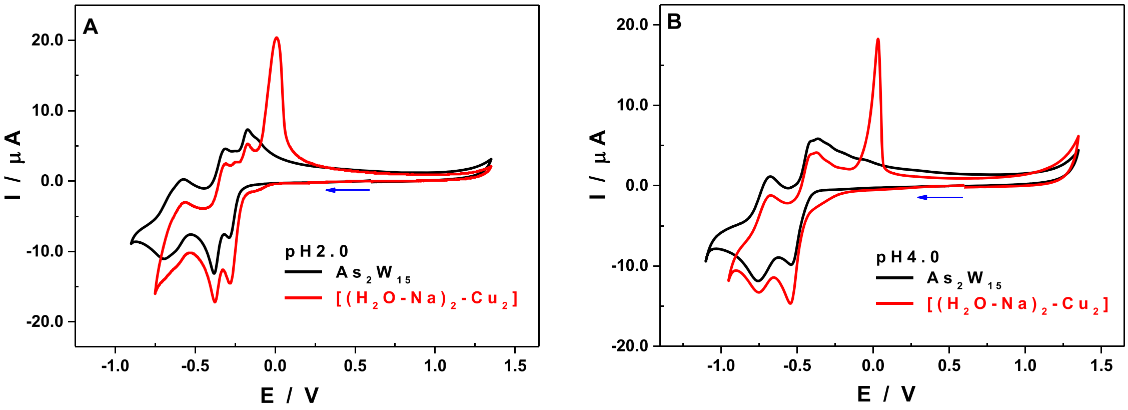

Fig. 4. CVs of **As_2W_{15}** (black) and **$[(H_2O-Na)_2-Cu_2]$** (red) recorded at a scan rate of 10 mV s^{-1} on an EPG electrode, in: (A) 0.2 M Li_2SO_4 + H_2SO_4 / pH 2.0; (B) 0.4 M CH_3COOLi + CH_3COOH / pH 4.0. Concentration of the bimetallic complexes: 0.2 mM. Concentration of **As_2W_{15}**: 0.4 mM.

working electrode surface as metallic Cu(0). Upon the reverse scan towards more positive potentials, Cu(0) is re-oxidised and reintegrated into its original coordination environments [36,40,51,64] This behaviour, previously reported in the literature, is further investigated using Electrochemical Quartz Crystal Microbalance (EQCM), as discussed in Section 3.3.

3.2.2. *Comparative study of $[(H_2O-Na)_2-Ni_2]$ and $[(H_2O-Na)_2-Cu_2]$ vs $[(H_2O-Ni)_2-Ni_2]$ and $[(H_2O-Cu)_2-Cu_2]$*

This section is dedicated to highlighting the differences in redox behaviour resulting from the substitution of Na^+ ions by Ni^{2+} or Cu^{2+} ions within complexes **$[(H_2O-Na)_2-Ni_2]$** and **$[(H_2O-Na)_2-Cu_2]$**, respectively. It is important to note that the equatorial metallic cluster remains homometallic; however, this substitution leads to a consequential increase in the number of "d" metal centres, specifically from two to four, and a variation of the total electrical charge from −18 to −16. The comparative analysis will be structured in two steps: the comparison between **$[(H_2O-Na)_2-Ni_2]$** and **$[(H_2O-Ni)_2-Ni_2]$** on the one hand, and between **$[(H_2O-Na)_2-Cu_2]$** and **$[(H_2O-Cu)_2-Cu_2]$** on the other hand, will be performed sequentially, first at pH 2.0 and subsequently at pH 4.0.

Concerning the homometallic Ni^{2+} based complexes, comparison of **$[(H_2O-Na)_2-Ni_2]$** and **$[(H_2O-Ni)_2-Ni_2]$** (Fig. 5) reveals that the redox behaviour is influenced by the overall electrical charge, which is directly

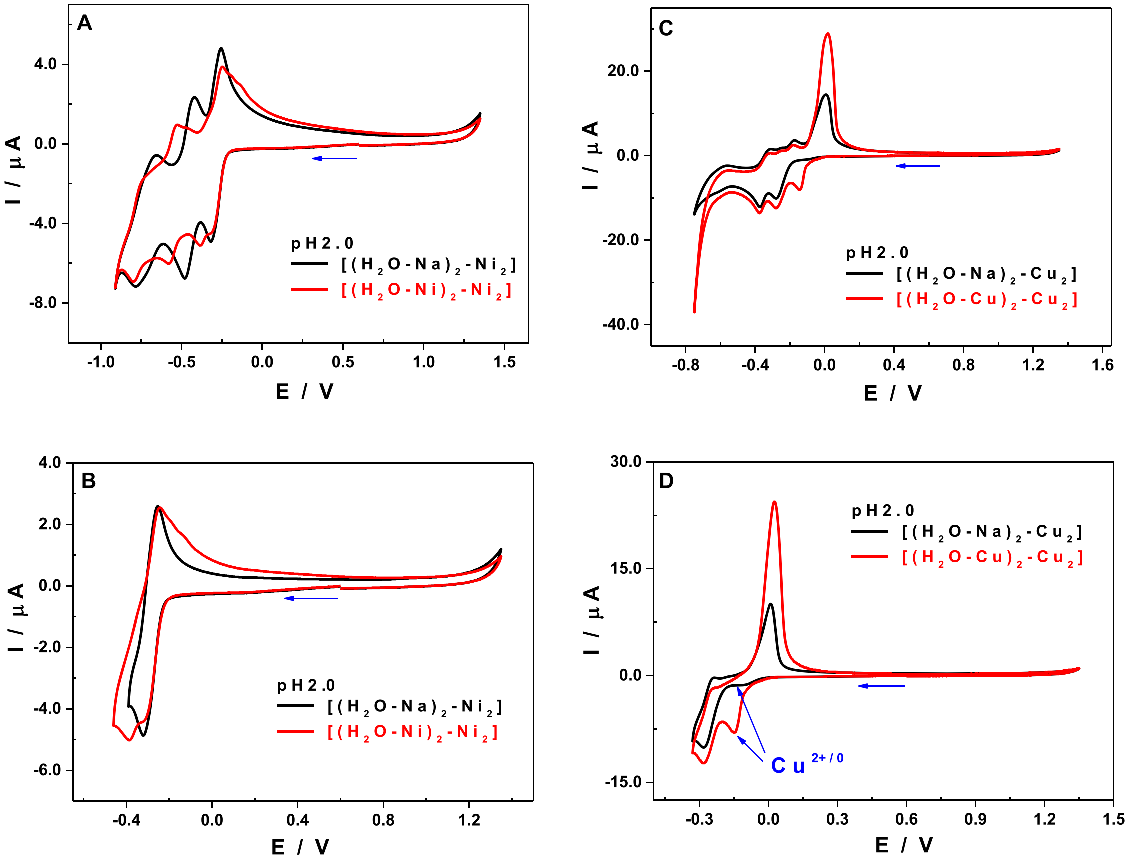

Fig. 5. CVs of **$[(H_2O-Na)_2-Ni_2]$** (black) and **$[(H_2O-Ni)_2-Ni_2]$** (red) recorded at 10 mV s^{-1} in pH 2.0 electrolyte (0.2 M Li_2SO_4 + H_2SO_4): (A) negative scan from +1.35 V to –0.91 V, (B) from +1.35 V to –0.39 V, both starting at +0.60 V. CVs of **$[(H_2O-Na)_2-Cu_2]$** (black) and **$[(H_2O-Cu)_2-Cu_2]$** (red) obtained under identical conditions: (C) scan from +1.35 V to –0.91 V, (D) from +1.35 V to –0.39 V, starting at +0.60 V.

related to the number of "d" metal centres sandwiched between the **As_2W_{15}** fragments. For **[(H_2O-Ni)$_2$-Ni$_2$]**, its CV at pH 2.0 differs from that of **[(H_2O-Na)$_2$-Ni$_2$]** in two main ways: 1) the first single reduction step splits into two distinct steps, and 2) subsequent reductions shift to more negative potentials. These effects are more pronounced at slower scan rates, as shown in Figures 5A, 5B, and S10.

The electrochemical behaviour of the complexes **[(H_2O-Na)$_2$-Cu$_2$]** and **[(H_2O-Cu)$_2$-Cu$_2$]** was investigated under identical experimental conditions (Figures 5C, 5D and S11). Although the Cu(II)-based reduction wave is not well defined for **[(H_2O-Na)$_2$-Cu$_2$]**, a distinctive re-oxidation wave, featuring a desorption process, is clearly observed during the reverse potential scan. A comparison of the desorption wave areas for the two compounds indicates that **[(H_2O-Cu)$_2$-Cu$_2$]** contains approximately twice as many Cu(II) centres as **[(H_2O-Na)$_2$-Cu$_2$]**. This assumption is further supported by EQCM measurements (Section 3.3).

Regarding the reduction processes associated with the reduction of W(VI) centres, both compounds display remarkably similar electrochemical profiles in terms of wave shape, potential position, and potential peak values. The reduction peak potentials for the first two steps are identical for both complexes, occurring at −0.28 V and −0.37 V vs. SCE (Table 3). Such an observation, which is consistent with expectations, can be rationalised by the fact that the reduction of Cu(II) centres in both systems leads to the formation of a comparable modified electrode surface, denoted Cu(0)@EPG. Simultaneously, the $[As_2W_{15}O_{56}]^{12-}$ fragments initially coordinated to the Cu(II) centres are released in the immediate vicinity of this newly formed EPG-modified surface.

It is therefore reasonable to assume that, following the reduction of Cu(II) to Cu(0), the subsequent reduction processes involve the same chemical species, namely, free $[As_2W_{15}O_{56}]^{12-}$, on an identical Cu(0)@EPG surface. The reduction peak potentials obtained are very close to those observed for $[As_2W_{15}O_{56}]^{12-}$ alone in solution (Table 2 and Fig. 4A), although slightly less negative. This modest positive shift suggests that the presence of Cu(0) at the EPG electrode surface facilitates the reduction of $[As_2W_{15}O_{56}]^{12-}$ under same experimental conditions.

The apparent absence of Cu(II) reduction in the CV of **[(H_2O-Na)$_2$-Cu$_2$]** compared to that observed for **[(H_2O-Cu)$_2$-Cu$_2$]** can be attributed to the differing coordination environments. In **[(H_2O-Cu)$_2$-Cu$_2$]**, the two supplementary Cu(II) centres, which occupy external coordination sites, are ligated by aqua groups, consequently being more easily reduced than the internal Cu(II) centres present in **[(H_2O-Na)$_2$-Cu$_2$]**. Conversely, the re-oxidation process for all Cu(0) species occurs at similar potentials. This suggests that, for both complexes, the re-oxidation involves the same desorption process of metallic copper, Cu(0), from the electrode surface. Furthermore, based on their coordination environment, the external Cu(II) centres are anticipated to exhibit a greater sensitivity to pH variations during the reduction process, which is consistent with the DFT results.

Upon adjusting the pH to 4.0 (0.4 M $CH_3COOLi + CH_3COOH$), a pronounced negative shift was observed for all reduction peaks, particularly those attributed to the cupric centres (Figures S12A and S12B) compared to the electrochemical behaviour reported at pH 2. These peaks merged with the reduction peaks of the W(VI) centres, appearing as shoulders (Fig. 6A). Consequently, it became challenging to isolate the reduction of the Cu(II) centres from the initial reduction step of the W(VI) centres (Figure S13A). Notably, the first reduction step of the tungsten centres exhibited a slight cathodic shift for **[(H_2O-Cu)$_2$-Cu$_2$]** compared to **[(H_2O-Na)$_2$-Cu$_2$]** ($\Delta E = 40$ mV). The most striking difference between the two compounds was evident during the anodic scan, upon re-oxidation of the deposited Cu(0). While **[(H_2O-Na)$_2$-Cu$_2$]** exhibited a single, symmetric re-oxidation peak, characteristic of a simple dissolution process, **[(H_2O-Cu)$_2$-Cu$_2$]** displayed at least two distinct re-oxidation peaks (Figures 6A and S13B). This complex behaviour suggests a multi-step re-oxidation mechanism involving either the formation of copper oxides/hydroxides or the intermediary of Cu(I) species.

Table 3
Peak potential (E_P) values (V vs. SCE) in 2 different media: pH 2.0 (0.2 M $Li_2SO_4 + H_2SO_4$) and pH 4.0 (0.4 M $CH_3COOLi + CH_3CCOH$).

pH 2.0						
		Cu	W_1	W_2	W_3	W_4
[(H_2O-Ni)$_2$-Ni$_2$]	E_{Pc}		−0.32	−0.38	−0.58	−0.70
	E_{Pa}		−0.13	−0.24	−0.53	−0.74
[(H_2O-Cu)$_2$Cu$_2$]	E_{Pc}	−0.15	−0.28	−0.37	−0.61	
	E_{Pa}	+0.03	−0.24	−0.31	−0.55	
pH 4.0						
		Cu	W_1	W_2	W_3	W_4
[(H_2O-Ni)$_2$Ni$_2$]	E_{Pc}		−0.61	−0.70	−091	
	E_{Pa}		−0.38	−0.61	−0.84	
[(H_2O-Cu)$_2$Cu$_2$]	E_{Pc}	−0.30	−0.57	−0.71		
	E_{Pa}	+0.10	+0.36	−0.37	−0.67	

The redox behaviour of **[(H_2O-Cu)$_2$-Cu$_2$]** should be greatly influenced by the properties of the medium of study. Two key factors are at play: first, the pH, set at 4.0, implies a hundred-fold lower H^+ ion concentration than in a previous medium at pH 2.0. Second, the nature of the electrolyte's anion is crucial. In fact, acetate ion is known for its coordinating power compared to the sulphate ion [65,66] These combined elements will have a direct impact on the reducibility of the external Cu(II) centres. These centres, each linked to a labile aqua group, will also exhibit acid-base properties. The synergy of all these factors will significantly influence the nature, formation and re-oxidation mechanisms, and the stability of the reduced species, particularly those adsorbed on the working electrode surface.

Upon increasing the pH from 2.0 to 4.0, the electrochemical behaviour of **[(H_2O-Na)$_2$-Ni$_2$]** and **[(H_2O-Ni)$_2$-Ni$_2$]** was dominated by changes in the redox processes associated with the W(VI) centres, as the Ni(II) centres remained electrochemically silent within the potential window. For the di-nickel complex, the reduction peaks associated with tungsten shifted cathodically as the pH increased from 2.0 to 4.0. At pH 2.0, two well-resolved peaks were observed whereas at pH 4.0 they merged into a single, broader feature consisting of a main peak at −0.62 V and a shoulder at −0.51 V vs. SCE (Figure S14A). A similar trend was observed for **[(H_2O-Ni)$_2$-Ni$_2$]** (Figure S14B). A direct comparison of the CVs at pH 4.0 (Fig. 6B) revealed that both compounds exhibited a similar initial reduction process, consisting of a shoulder around −0.50 V followed by a well-defined main peak near −0.62 V for **[(H_2O-Na)$_2$-Ni$_2$]** and −0.61 V for **[(H_2O-Ni)$_2$-Ni$_2$]**. Additionally, **[(H_2O-Ni)$_2$-Ni$_2$]** displayed an intermediate reduction peak at −0.70 V. Both compounds exhibited a final reduction process at approximately −0.90 V vs. SCE.

Comparisons between the CVs of **As_2W_{15}** and the homometallic compounds, recorded at a scan rate of 10 mV s^{-1}, are presented in Figure S15. As for the compounds previously described containing two d-metal centres in the equatorial cluster, the CVs obtained at higher scan rates for those containing four d-metal centres (Figures S16 and S17) exhibit similar redox characteristics. This suggests that the underlying electrochemical processes are fundamentally the same, regardless of the scan rate.

3.2.3. Comparative electrochemical study of [(H_2O-Na)$_2$-Ni$_2$], [(H_2O-Na)$_2$-Cu$_2$], [(H_2O-Ni)$_2$-Ni$_2$] and [(H_2O-Cu)$_2$-Cu$_2$] vs [(H_2O-Cu)$_2$-Ni$_2$] and [(H_2O-Ni)$_2$-Cu$_2$]

In previous sections, our focus was put on sandwich-type complexes featuring homometallic equatorial clusters composed exclusively of either Ni(II) or Cu(II) centres. The findings from these studies revealed that accumulating "d" metal centres into the equatorial cluster, specifically by expanding from two to four centres, exerts a direct or indirect influence on the complex's overall redox behaviour. This phenomenon of electrochemical interdependence is particularly significant because it was observed even when the metals incorporated into the equatorial cluster are intrinsically electrochemically silent within the potential

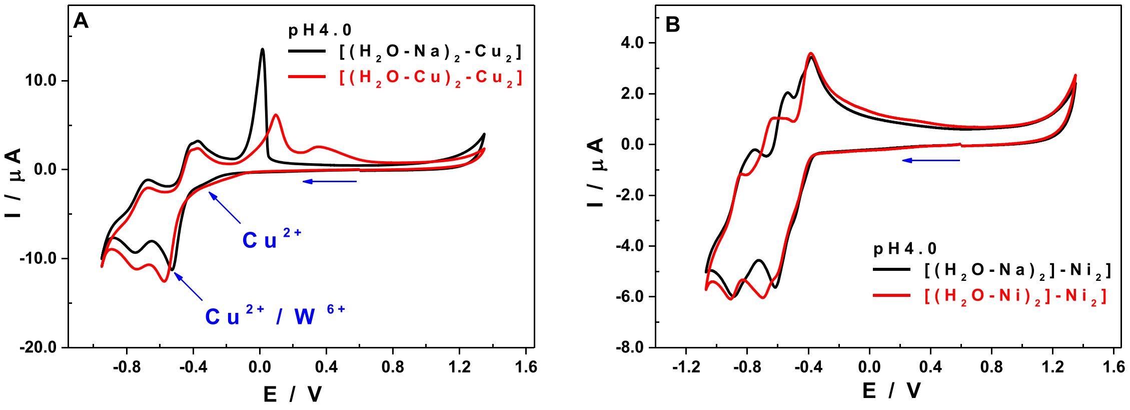

Fig. 6. CVs obtained at a scan rate of 10 mV s^{-1} in a pH 4.0 acetate buffer (0.4 M CH_3COOLi + CH_3COOH). POM concentration: 0.2 mM. (A) CVs of **[(H$_2$O-Na)$_2$-Cu$_2$]** (black) and **[(H$_2$O-Cu)$_2$-Cu$_2$]** (red). (B) CVs of **[(H$_2$O-Na)$_2$-Ni$_2$]** (black) and **[(H$_2$O-Ni)$_2$-Ni$_2$]** (red). Working electrode, EPG. Counter electrode, Pt. reference electrode, SCE.

window under investigation. This compelling observation strongly suggests the existence of intra-cluster electronic coupling or inductive effects that effectively modulate the reactivity of the active centres, even in the absence of a direct redox process involving the silent centres themselves [29]

This section extends our investigation to heterometallic sandwich complexes, incorporating both Ni(II) and Cu(II) centres within the equatorial cluster. Specifically, we will examine the electrochemical behaviour of **[(H$_2$O-Cu)$_2$-Ni$_2$]** and **[(H$_2$O-Ni)$_2$-Cu$_2$]**.

The first objective of this section is to elucidate the impact of substituting Na$^+$ with either Cu^{2+} or Ni^{2+}, respectively, on the cyclic voltammograms (CVs) of **[(H$_2$O-Na)$_2$-Ni$_2$]** and **[(H$_2$O-Na)$_2$-Cu$_2$]**. Subsequently, we will conduct a comparative analysis of the redox properties of saturated sandwich complexes, which possess four "d" metal centres, either identical or different, within the equatorial cluster.

a) [(H$_2$O-Na)$_2$-Ni$_2$] and [(H$_2$O-Na)$_2$-Cu$_2$] vs [(H$_2$O-Cu)$_2$-Ni$_2$] and [(H$_2$O-Ni)$_2$-Cu$_2$].

The substitution of the Na$^+$ ions in **[(H$_2$O-Na)$_2$-Ni$_2$]** with Cu^{2+} ions, positioned at external sites and coordinated to water molecules, resulted in the appearance of a new reduction wave in the CV of **[(H$_2$O-Cu)$_2$-Ni$_2$]** at a less negative potential compared to the reduction waves associated with the W(VI) centres (Fig. 7A). This new feature can be

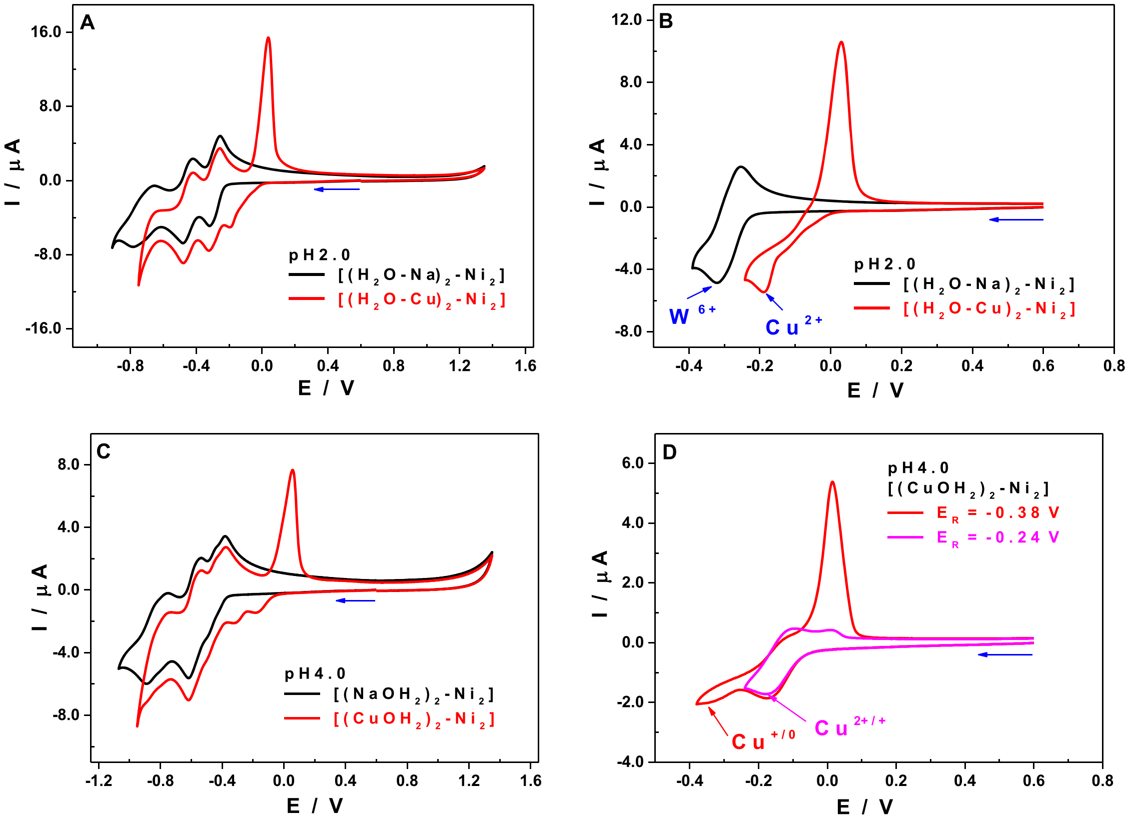

Fig. 7. CVs recorded at 10 mV s^{-1} for 0.2 mM POM solutions in (A–B) pH 2.0 (0.2 M Li_2SO_4 + H_2SO_4) and (C–D) pH 4.0 (0.4 M CH_3COOLi + CH_3COOH) electrolytes. (A) Scans from +0.60 V to –0.91 V for **[(H$_2$O-Na)$_2$-Ni$_2$]** and –0.75 V for **[(H$_2$O-Cu)$_2$-Ni$_2$]**. (B) Expanded view of scans from + 0.60 V to –0.39 V for **[(H$_2$O-Na)$_2$-Ni$_2$]** and –0.24 V for **[(H$_2$O-Cu)$_2$-Ni$_2$]**. (C) Negative scans from +1.35 V to –1.10 V for **[(H$_2$O-Na)$_2$-Ni$_2$]** (black) and –0.95 V for **[(H$_2$O-Cu)$_2$-Ni$_2$]** (red), starting at +0.60 V. (D) CVs of **[(H$_2$O-Cu)$_2$-Ni$_2$]** showing negative scans from +0.60 V to –0.38 V (red) and –0.24 V (violet).

unequivocally assigned to the reduction of the Cu(II) centres, which are known to undergo reduction prior to the tungsten centres in polyoxometalates, as described above and in previous studies [51] Unlike **[(H$_2$O-Na)$_2$-Cu$_2$]** and **[(H$_2$O-Cu)$_2$-Cu$_2$]**, the reduction peaks of the Cu (II) and W(VI) centres are well resolved for **[(H$_2$O-Cu)$_2$-Ni$_2$]** (Figures 7B and S17). Beyond the first two quasi-reversible reduction steps of the tungsten centres, a significant enhancement in the reduction current and a loss of reversibility were observed for the third step, suggesting an electrocatalytic process, most likely the HER. This hypothesis will be the scope of a future paper that will address electrocatalytic properties of these complexes. During the reverse scan, a prominent symmetric desorption peak was observed, confirming the previous adsorption of metallic copper on the electrode surface. The desorption potential of Cu(0) was consistent with that observed for other Cu^{2+}-containing compounds, occurring at approximately 0.05 V vs. SCE.

When the two Na^+ ions in the compound **[(H$_2$O-Na)$_2$-Cu$_2$]** are substituted by Ni^{2+} ions, significant modifications are observed in the CV of the resulting compound, **[(H$_2$O-Ni)$_2$-Cu$_2$]**, compared to the initial unsubstituted compound. Fig. 8 presents the CVs of both compounds in a 0.2 M Li_2SO_4 + H_2SO_4 / pH 2.0 medium. On the CV of the compound **[(H$_2$O-Ni)$_2$-Cu$_2$]** (red), the wave attributed to the reduction of the two Cu(II) centres has become much larger and appears at less negative potentials compared to the initial compound, **[(H$_2$O-Na)$_2$-Cu$_2$]** (black). Furthermore, the results of the Controlled Potential Coulometry (CPC) confirm that both compounds contain the same number of Cu(II) centres (see ESI). Therefore, we propose the following hypotheses to explain this difference: 1) Replacing Na^+ ions by Ni^{2+} decreases the overall negative charge of the complex from −18 to −16, thus accepting additional electrons more easily than the initial complex, i.e., at less negative potentials. This effect will be particularly felt at the level of the equatorial metallic cluster containing the Cu(II) centres, which will receive these first electrons. 2) The second hypothesis is that of steric hindrance. Indeed, Ni^{2+}, being larger than Na^+, and having taken its place, will influence the response of the Cu(II) centres, which, while remaining in internal sites, will be more accessible than when they were associated with the Na(I) centres. As in the case of **[(H$_2$O-Cu)$_2$-Ni$_2$]**, the CV of **[(H$_2$O-Ni)$_2$-Cu$_2$]** shows that the reduction wave attributed to the Cu(II) centres is much more pronouncedly separated from the waves attributed to the reduction of the W(VI) centres (Fig. 8). The substitution of Na^+ by Ni^{2+} allows the reduction of the Cu(II) centres in the internal position to be separated from that of the tungsten skeleton. They also induce notable modifications on the redox processes attributed to the W(VI) centres. Indeed, we observe on the CV of **[(H$_2$O-Ni)$_2$-Cu$_2$]** (Fig. 8), an additional reduction step at −0.63 V vs. SCE, which was not present in **[(H$_2$O-Na)$_2$-Cu$_2$]**. This behaviour of multiplying the reduction waves of the W(VI) centres has already been observed above when we moved from **[(H$_2$O-Na)$_2$-Ni$_2$]** with two Ni(II) centres in internal sites to **[(H$_2$O-Ni)$_2$-Ni$_2$]**, with two additional Ni(II) centres in external sites (vide supra, Fig. 5A).

Next, we evaluate whether the substitution of Na^+ ions by either Cu^{2+} or Ni^{2+} ions exerts a comparable influence on the redox behaviour of the new POM under higher pH conditions (pH 4.0) in a lithium acetate medium.

In a 0.4 M CH_3COOLi + CH_3COOH medium at pH 4.0 (Fig. 7C), when comparing the CVs of the two compounds **[(H$_2$O-Na)$_2$-Ni$_2$]** (black) and **[(H$_2$O-Cu)$_2$-Ni$_2$]** (red), the separation of the redox processes attributable to the Cu(II) centres from those of the W(VI) centres remains as clear as the one observed earlier at pH 2.0. Moreover, the reduction of

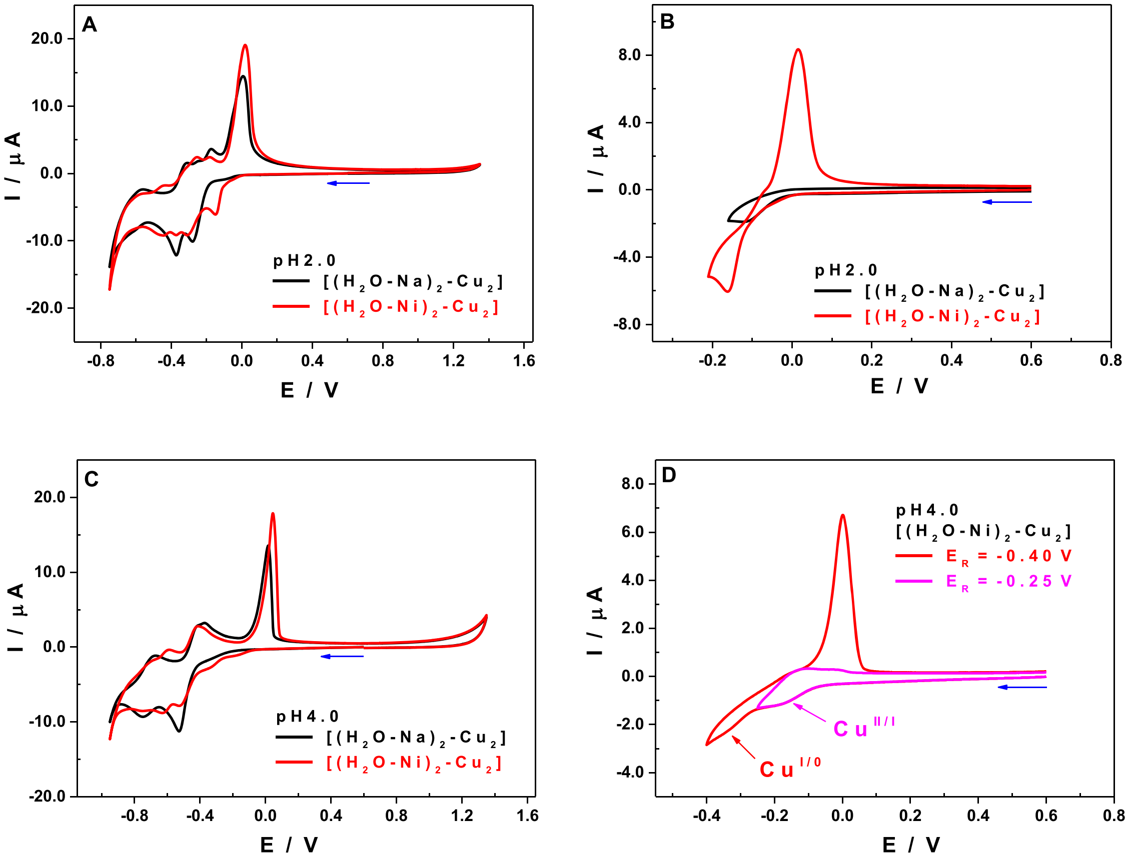

Fig. 8. CVs of **[(H$_2$O-Na)$_2$-Cu$_2$]** (black) and **[(H$_2$O-Ni)$_2$-Cu$_2$]** (red) recorded at 10 mV s^{-1} in pH 2.0 electrolyte (0.2 M Li_2SO_4 + H_2SO_4) and pH 4.0 electrolyte (0.4 M CH_3COOLi + CH_3COOH). (A-B) pH 2.0: (A) negative scans from +1.35 V to –0.75 V, starting at +0.60 V; (B) expanded scans from +0.60 V to –0.16 V for **[(H$_2$O-Na)$_2$-Cu$_2$]** and –0.21 V for **[(H$_2$O-Ni)$_2$-Cu$_2$]**. (C-D) pH 4.0: (C) negative scans from +1.35 V to –0.95 V, starting at +0.60 V, for both compounds; (D) CVs of **[(H$_2$O-Ni)$_2$-Cu$_2$]** showing scans from +0.60 V to –0.40 V (red) and –0.25 V (violet).

the two cupric centres occurs in two well-defined steps that can be isolated (Fig. 7D). This operation shows us that the two Cu(II) centres are reduced in two steps, going through a first step, Cu(II) → Cu(I), with a reduction peak potential at −0.18 V vs. SCE and an oxidation peak potential at −0.09 V vs. SCE. The second reduction step, which occurs at −0.33 V vs. SCE, Cu(I) → Cu(0), occurs with copper adsorption on the working electrode surface, leading to the appearance of a desorption wave with an anodic peak at +0.10 V vs. SCE. Although the H^+ concentration in this medium is at least 100 times lower compared to the pH 2.0 medium (Fig. 7A)

Similar observations are made when comparing the CVs of the compounds **$[(H_2O\text{-}Na)_2\text{-}Cu_2]$** and **$[(H_2O\text{-}Ni)_2\text{-}Cu_2]$**. Although the Cu (II) centres are still in internal sites, they are reduced more easily when associated with Ni(II) centres than when associated with Na(I) centres (Fig. 8C). The hypotheses made in the 0.2 M $Li_2SO_4 + H_2SO_4$ medium at pH 2.0 are equally valid in this case. Moreover, even if the shift between the reduction waves of the Cu(II) and W(VI) centres is less pronounced than in the case of the compound **$[(H_2O\text{-}Cu)_2\text{-}Ni_2]$** where copper is in external sites, we still observe distinctly the two reduction steps of the two Cu(II) centres in external positions: Cu(II) → Cu(I), when the potential scan is stopped at −0.25 V vs. SCE, and Cu(I) → Cu(0), when going down to −0.4 V vs. SCE (Fig. 8D). This is impossible in the absence of Ni(II) centres, as is the case of the compound **$[(H_2O\text{-}Na)_2\text{-}Cu_2]$**.

Similarly, as observed in 0.2 M $Li_2SO_4 + H_2SO_4$ at pH 2.0, a new reduction wave of the W(VI) centres appears on the CV of **$[(H_2O\text{-}Ni)_2\text{-}Cu_2]$** with a peak potential at −0.63 V vs. SCE (Fig. 8C, Table 4).

The CVs recorded at higher scan rates (Figures S19) present similar features, indicating that the electrochemical processes involved for the two new sandwich compounds are essentially the same, independent of the kinetics imposed by the scan rate.

In conclusion, regardless of the solution pH (2 or 4) and the nature of the supporting electrolyte (lithium sulphate or lithium acetate), the joint incorporation of Cu(II) and Ni(II) centres within the equatorial cluster of the two newly synthesised sandwich-type POMs leads to pronounced and significant modifications in their redox behaviour. These changes cannot be solely ascribed to variations in the overall electrical charge of the cluster; rather, they arise from a specific electronic synergy between the Cu(II) and Ni(II) centres, which becomes evident only when both metals are co-localised within the same structural framework.

DFT calculations provide further insight through the electronic structure variations underlying the experimentally observed redox features. This cooperative effect, already hinted at in related systems, [29] is more clearly demonstrated and rationalised herewith through the combined experimental and theoretical analysis.

b) $[(H_2O\text{-}Cu)_2\text{-}Cu_2]$ vs $[(H_2O\text{-}Cu)_2\text{-}Ni_2]$ and $[(H_2O\text{-}Ni)_2\text{-}Cu_2]$.

In the previous section, we investigated the redox behaviour of the two mixed Ni-Cu sandwich complexes, **$[(H_2O\text{-}Cu)_2\text{-}Ni_2]$ and $[(H_2O\text{-}Ni)_2\text{-}Cu_2]$**, by tracing their structural lineage, that is, by comparing them with their homonuclear analogues **$[(H_2O\text{-}Na)_2\text{-}Ni_2]$ and $[(H_2O\text{-}Na)_2\text{-}Cu_2]$**, which feature Na(I) centres in the outer positions. This analysis allowed us to highlight the evolution of their redox properties resulting from the substitution of the two Na(I) centres by either Ni(II) or Cu(II) centres, depending on the system considered.

In the present section, the comparison focuses directly on the three copper-containing compounds whose equatorial metallic cluster comprises four d-metal centres, namely: **$[(H_2O\text{-}Cu)_2\text{-}Cu_2]$, $[(H_2O\text{-}Cu)_2\text{-}Ni_2]$ and $[(H_2O\text{-}Ni)_2\text{-}Cu_2]$**.

A direct comparison of the CVs of these three compounds (Fig. 9) allows several key observations to be made.

First, at pH 2.0: the presence of Ni(II) centres in the outer positions exerts a pronounced influence on the redox wave associated with the Cu (II) centres located internally. The latter become better defined, and two distinct reduction steps can be clearly differentiated from the reduction process involving the W(VI) centres (red CV, Fig. 9A).

Furthermore, the comparison of the CV of **$[(H_2O\text{-}Ni)_2\text{-}Cu_2]$** (red curve) with that of **$[(H_2O\text{-}Cu)_2\text{-}Ni_2]$** (blue curve) reveals that the Cu(II) centres, although located in inner positions in the first one, appear to be more easily reduced when coordinated to Ni(II) centres (Fig. 9B). This seemingly counterintuitive behaviour can be more clearly interpreted through DFT calculations, which help elucidate the underlying electronic factors governing this phenomenon.

As expected, the CV of the compound containing four Cu(II) centres (black curve) displays the highest reduction currents for the processes involving the cupric centres. Also, when comparing the reduction peak currents associated with Cu(II) centres in **$[(H_2O\text{-}Ni)_2\text{-}Cu_2]$ and $[(H_2O\text{-}Cu)_2\text{-}Ni_2]$**, higher current intensities are observed for the former (red curve). However, a meaningful comparison requires consideration of the integrated areas of the overall redox waves. Analysis of these areas, corresponding to the total reduction of Cu(II) centres according to electrochemical Eq. (1), reveals a ratio of 2:2:4 for the three compounds **$[(H_2O\text{-}Ni)_2\text{-}Cu_2]$, $[(H_2O\text{-}Cu)_2\text{-}Ni_2]$** and **$[(H_2O\text{-}Cu)_2\text{-}Cu_2]$**, respectively. These results are in excellent agreement with those obtained from CPC (ESI) and EQCM (vide infra) measurements.

$$Cu^{2+} + 2e^- \rightleftharpoons Cu^0 \tag{1}$$

The trend observed at pH 2.0, where the Cu(II) centres of **$[(H_2O\text{-}Cu)_2\text{-}Ni_2]$** appeared to be the least easily reduced, is reversed at pH 4.0. At this higher pH, these Cu(II) centres become more readily reducible than those of their analogue **$[(H_2O\text{-}Ni)_2\text{-}Cu_2]$**, as might be expected based on their electronic environment. Even more intriguing, for both mixed Cu–Ni sandwich-type compounds, the Cu(II) centres are reduced more easily than the four Cu(II) centres of the homonuclear complex **$[(H_2O\text{-}Cu)_2\text{-}Cu_2]$** (Figures 9A and S20).

Within the potential window explored (+1.35 V to –0.40 V vs. SCE), the two Cu(II) centres of the so-called “mixed saturated” or heteronuclear compounds **$[(H_2O\text{-}Cu)_2\text{-}Ni_2]$** and **$[(H_2O\text{-}Ni)_2\text{-}Cu_2]$** undergo full reduction to the metallic Cu(0) state, according to the electrochemical Eq. (1). In contrast, the reduction of the Cu(II) centres in the homonuclear compound **$[(H_2O\text{-}Cu)_2\text{-}Cu_2]$** proceeds only to the Cu(I) state, as described by Eq. (2). To achieve complete reduction to Cu(0), more negative potentials are required, overlapping with the onset of the first reduction process of the W(VI) centres (Fig. 9D and S13).

This observation strongly supports the hypothesis of a synergistic interaction between Ni(II) and Cu(II) centres, which facilitates the reduction of the latter. Such a cooperative electronic effect between heterometallic sites appears to be a key factor underlying the enhanced redox activity observed in these mixed-metal sandwich complexes.

$$Cu^{2+} + e^- \rightleftharpoons Cu^+ \tag{2}$$

$$Cu^+ + e^- \rightleftharpoons Cu^0 \tag{3}$$

Balance :

Table 4
Peak potential (E_P) values in 2 different media: pH 2.0 (0.2 M $Li_2SO_4 + H_2SO_4$) and pH 4.0 (0.4 M $CH_3COOLi + CH_3COOH$).

pH 2.0		Cu_1	Cu_2	W_1	W_2	W_3
$[(H_2O\text{-}Cu)_2\text{-}Ni_2]$	E_{Pc}	−0.12	−0.19	−0.33	−0.48	−0.70
	E_{Pa}	+0.03		−0.25	−0.42	−0.64
$[(H_2O\text{-}Ni)_2\text{-}Cu_2]$	E_{Pc}	−0.12	−0.20	−0.30	−0.37	−0.61
	E_{Pa}	+0.04		−0.26	−0.34	−0.58
pH 4.0		Cu_1	Cu_2	W_1	W_2	W_3
$[(H_2O\text{-}Cu)_2\text{-}Ni_2]$	E_{Pc}	−0.18	−0.33	−0.50	−0.62	−0.87
	E_{Pa}	−0.09	+0.01	−0.44	−0.54	−0.76
$[(H_2O\text{-}Ni)_2\text{-}Cu_2]$	E_{Pc}	−0.20	−0.35	−0.54	−0.63	−0.75
	E_{Pa}	−0.10	0.00	−0.41	−0.58	−0.70

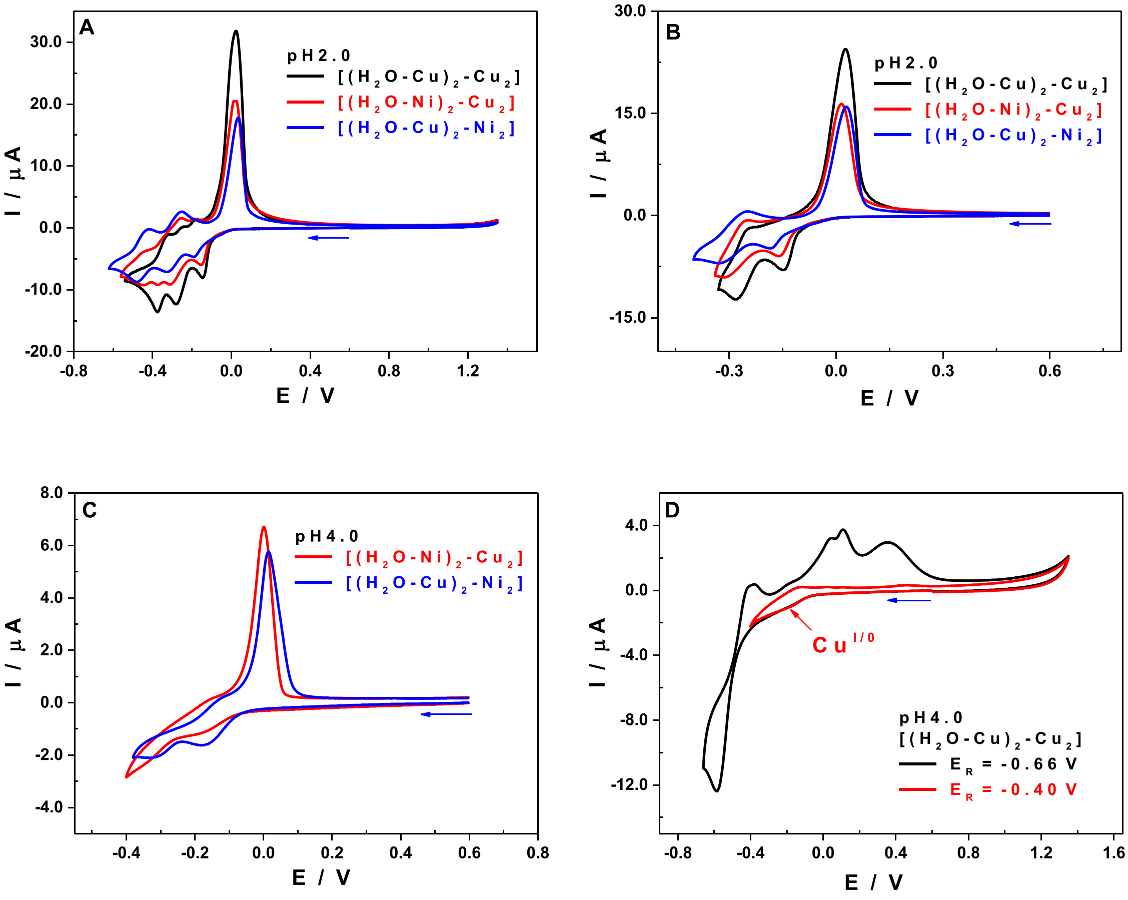

26

Fig. 9. CVs of **[(H$_2$O-Cu)$_2$-Cu$_2$]** (black), **[(H$_2$O-Ni)$_2$-Cu$_2$]** (red), and **[(H$_2$O-Cu)$_2$-Ni$_2$]** (blue) recorded at 10 mV s^{-1} in pH 2.0 electrolyte (2 M Li$_2$SO$_4$ + H$_2$SO$_4$) and pH 4.0 electrolyte (0.4 M CH$_3$COOLi + CH$_3$COOH). (A-B) pH 2.0: (A) potential scans extended to the second reduction step of W(VI) centres; (B) scans restricted to the first reduction step of W(VI) centres. (C-D) pH 4.0: (C) CVs of **[(H$_2$O-Ni)$_2$-Cu$_2$]** (red) and **[(H$_2$O-Cu)$_2$-Ni$_2$]** (blue); (D) CVs of **[(H$_2$O-Cu)$_2$-Cu$_2$]** showing scans down to the first reduction step of W(VI) centres (black) and restricted to the first reduction step of Cu(II) centres (red).

$$Cu^{2+} + 2e^{-} \rightleftharpoons Cu^{0} \qquad (4)$$

3.3. *Electrochemical quartz crystal microbalance (EQCM)*

Electrochemical Quartz Crystal Microbalance (EQCM) was employed in combination with other electrochemical techniques, to characterise the four copper-containing compounds and to gain a deeper understanding of the redox behaviour of the Cu(II) centres present in the various POMs. EQCM, like XPS, allows for quantitative characterisation of the Cu(II) centres.

The working principle of the EQCM is based on monitoring the variations in the oscillation frequency of a quartz crystal that serves as the working electrode in the experimental setup. Any mass deposition on the electrode surface leads to a decrease in the crystal's resonance frequency, whereas desorption or dissolution of adsorbed species results in a frequency increase. This correlation enables real-time monitoring of the formation and dissolution of deposits on the working electrode surface during electrochemical processes, using techniques such as cyclic voltammetry (CV) or controlled-potential coulometry (CPC), among others.

To maintain a working electrode composition comparable to that employed in previous electrochemical experiments, the quartz crystal sensors were coated with glassy carbon instead of edge-plane pyrolytic graphite. All other experimental parameters were kept constant, particularly the electrolyte composition and concentration, consisting of 0.4 M CH$_3$COOLi + CH$_3$COOH at pH 4.0. Low potential scan rates (5 mV s^{-1}) were initially applied to promote, whenever applicable, the nucleation and deposition of metallic copper (Cu^0) on the working electrode surface. The counter and reference electrodes remained the same, namely Pt and SCE.

The first comparison was established between the two heterometallic compounds, **[(H$_2$O-Ni)$_2$-Cu$_2$]** and **[(H$_2$O-Cu)$_2$-Ni$_2$]**. Their CVs recorded in 0.4 M CH$_3$COOLi + CH$_3$COOH at pH 4.0 show that the reduction of the Cu(II) centres occurs over approximately the same potential range, between 0.0 and –0.43 V vs. SCE. However, since the separation between the reduction processes of Cu(II) and W(VI) centres is not clearly defined, it cannot be concluded that the reduction of all Cu(II) centres is complete at the end of the cathodic waves assigned to copper. This process may continue slightly beyond that range and overlap with the first reduction step of the W(VI) centres. Consequently, the copper content in these compounds cannot be accurately quantified based solely on the analysis of the CV or CPC data.

For this reason, in the present study, the potential scan was extended to the first reduction wave associated with the W(VI) centres, i.e., down to –0.70 V vs. SCE. The variation of the quartz crystal's oscillation frequency, which constitutes the working electrode, was monitored as a function of the applied potential. The resulting frequency variation–potential curves can thus be directly compared with the CVs of the corresponding compounds, recorded simultaneously. Because the oscillation frequency of quartz is inherently constant, any decrease in frequency indicates the formation of a deposit on the electrode surface. This approach enables precise determination, for each compound, of the potential at which the electrochemical reaction corresponding to the formation of metallic copper, Cu(0), begins.

The potential values corresponding to the onset of Cu(0) deposition, denoted as E_{ONSET} -EQCM, are consistently more negative than those associated with the onset of Cu(II) reduction (E_{ONSET} -CV), which are determined at the foot of the Cu-related cathodic wave in the CV (Table 5). This observation supports the hypothesis that, for all the studied compounds, the Cu(II) centres are reduced through two successive steps, as described by Eqs. (2) and (3) above, steps that remain difficult to distinguish in conventional cyclic voltammetry.

Returning to the comparison between **[(H$_2$O-Ni)$_2$-Cu$_2$]** and **[(H$_2$O-Cu)$_2$-Ni$_2$]**, their CVs show that the first reduction step of Cu(II) centres begins at very similar potentials, slightly more negative for **[(H$_2$O-Ni)$_2$-Cu$_2$]** (–0.07 V vs. SCE) than for **[(H$_2$O-Cu)$_2$-Ni$_2$]** (–0.05 V vs. SCE), representing a shift of approximately 20 mV (Table 5 and Fig. 10A). This difference, already noted and discussed earlier, is confirmed here. Regarding the second reduction step, corresponding to the formation and deposition of Cu(0) on the working electrode surface, the EQCM frequency-potential profiles (Fig. 10B) clearly reveal the Cu(0) deposition on the glassy carbon electrode, providing deeper insight into the deposition and redissolution phenomena occurring during the forward and reverse scans, respectively.

The onset of Cu(0) deposition, identified as the potential where the quartz frequency starts to decrease, exhibits a potential shift consistent with that observed in the CVs for Cu(II) reduction. However, this shift is significantly larger, approximately five times greater, corresponding to 100 mV, ranging from −0.38 V vs. SCE for **[(H$_2$O-Ni)$_2$-Cu$_2$]** to –0.28 V vs. SCE for **[(H$_2$O-Cu)$_2$-Ni$_2$]**. These potentials define the threshold at which reaction (3) begins. The frequency decrease continues up to the potential inversion point (−0.70 V vs. SCE) and even slightly beyond, as the scan direction reverses toward more positive potentials.

The persistence of a low oscillation frequency beyond the Cu(II) reduction region, extending into the first reduction step of W(VI) centres, is expected since these potentials are significantly more negative than those required for the complete reduction of Cu(II) to Cu(0). Under such conditions, copper can only exist in the metallic state. Similarly, during the reverse (anodic) scan, the quartz frequency remains below the initial deposition threshold values observed earlier (−0.38 V vs. SCE for **[(H$_2$O-Ni)$_2$-Cu$_2$]** and −0.25 V vs. SCE for **[(H$_2$O-Cu)$_2$-Ni$_2$]**).

A subsequent frequency increase is observed only when the potential reaches −0.14 V vs. SCE, suggesting that this potential corresponds to the onset of Cu(0) re-oxidation. This threshold, identical for both compounds, is not preceded by a plateau that would indicate a latency region in which the preformed deposit remains stable. Instead, the frequency variation indicates the initiation of redissolution at this potential. Taking the frequency value at the initial potential of the CV (+0.60 V) as the reference, the total frequency variation of the quartz crystal, which serves as the working electrode, is nearly identical for both compounds (Table 5), indicating an equivalent number of reducible Cu(II) centres in each.

A comparative analysis of the CVs of **[(H$_2$O-Na)$_2$-Cu$_2$]** and **[(H$_2$O-Ni)$_2$-Cu$_2$]** (Fig. 10C and D) provides compelling experimental support for our previously formulated hypotheses regarding the redox behaviour of these mixed-metal POMs. As shown in Fig. 10C, substitution of the two Na$^+$ ions with Ni^{2+} induces a pronounced anodic shift of approximately 260 mV in the onset potential of electrochemical process (2). At first glance, the higher current intensity and enlarged peak area observed for **[(H$_2$O-Ni)$_2$-Cu$_2$]** might suggest an increased concentration of Cu(II) redox centres relative to **[(H$_2$O-Na)$_2$-Cu$_2$]**.

Table 5

Onset potentials for the reduction of Cu(II) centres, Eq. (2), ONSET-CV, and for copper deposition, Eq. (3), ONSET-EQCM, obtained respectively from the CV and the EQCM curves. This table also presents the maximum frequency variations and their ratios, which reflect the ratios of the number of Cu(II) centres in the different compounds.

	ONSET-CV / V	ONSET-EQCM / V	ΔF / Hz	Ratio Cu(II)
[(H$_2$O-Na)$_2$-Cu$_2$]	−0.33	−0.52	−625	1.000
[(H$_2$O-Cu)$_2$-Cu$_2$]	−0.10	−0.36	−1354	2.166
[(H$_2$O-Ni)$_2$-Cu$_2$]	−0.07	−0.38	−677	1.083
[(H$_2$O-Cu)$_2$-Ni$_2$]	−0.05	−0.28	−674	1.078

However, such an interpretation is contradicted by the EQCM data. The EQCM frequency variation ratio between the two compounds is 1.08 (Table 5), which unequivocally indicates that both systems contain an equivalent number of Cu(II) centres. This crucial information demonstrates the complementary and indispensable role of EQCM in validating the quantitative aspects of redox-active species, as the CV data alone can be misleading due to overlapping. Therefore, the observed anodic shifts in both the CV onset (ONSET–CV) and the corresponding frequency response (ONSET–EQCM) can be ascribed exclusively to the presence of Ni(II) centres, which promote the initial reduction of Cu(II) sites through an electronic and structural modulation of the POM framework.

A similar trend is observed when comparing **[(H$_2$O-Na)$_2$-Cu$_2$]** with its homologue containing four Cu(II) centres, **[(H$_2$O-Cu)$_2$-Cu$_2$]**. As illustrated in Fig. 10E, the onset potential of reaction (2) shifts anodically by 230 mV, while Fig. 10F shows a 160 mV anodic shift for reaction (3). These systematic potential shifts can be rationalised by two concurrent effects: (i) the incorporation of two additional Cu(II) centres occupying external coordination sites, and (ii) a concomitant decrease in the overall negative charge of the POM framework, which stabilises higher oxidation states. The EQCM frequency ratio between these two compounds (ΔF ratio = 2.166) confirms a 4:2 ratio of Cu(II) centres, thereby providing direct gravimetric evidence that complements the electrochemical findings and firmly establishes the stoichiometric correspondence between the redox events and the number of active Cu(II) sites.

Further comparative analyses, namely, **[(H$_2$O-Cu)$_2$-Ni$_2$]** and **[(H$_2$O-Cu)$_2$-Cu$_2$]**, **[(H$_2$O-Ni)$_2$-Cu$_2$]** and **[(H$_2$O-Cu)$_2$-Cu$_2$]**, **[(H$_2$O-Na)$_2$-Cu$_2$]** and **[(H$_2$O-Ni)$_2$-Cu$_2$]**, are presented in the Supporting Information (Figures S21). Collectively, these data reinforce the conclusions summarised in Table 5. Regardless of whether Ni(II) ions occupy internal or external coordination sites, their presence consistently facilitates the initial reduction of Cu(II) centres by lowering the corresponding activation barrier.

Regarding the subsequent reduction process associated with copper metal deposition at the electrode surface [Eq. (3)], the relative ease of Cu deposition follows the order: **[(H$_2$O-Cu)$_2$-Ni$_2$]** > **[(H$_2$O-Cu)$_2$-Cu$_2$]** > **[(H$_2$O-Ni)$_2$-Cu$_2$]** > **[(H$_2$O-Na)$_2$-Cu$_2$]**. Remarkably, copper desorption (re-oxidation) occurs at nearly identical potentials (−0.15 V to −0.14 V vs. SCE) for all compounds, indicating that this step is largely independent of the POM composition.

Finally, the excellent agreement between the EQCM-derived mass variations and **XPS** data further validates the proposed stoichiometries and the distribution of Cu(II) centres within the various POM structures. Taken together, the combined use of CV and EQCM offers a powerful, synergistic approach for disentangling complex redox mechanisms in multi-metallic POM systems and for accurately correlating electrochemical responses with structural and compositional parameters.

4. Theoretical study

4.1. Structural aspects

Sandwich POMs are supported by the robust tungsten oxide $(W_{15}O_{56})_2$ framework, with computed terminal and bridging W–O bond distances within the 2.015 to 2.135 Å range, typical values for polyoxotungstates. The present computational analysis mostly focuses on the equatorial region, where the Cu, Ni and Na atoms are located. In systems containing external Ni atoms, the Ni–O$_{(wat)}$ bond distances (O$_{(wat)}$ = oxygen from H_2O) were consistently computed to be around 2.2 Å (see Fig. 11 and Table S3), like other M-O bond distances such as those

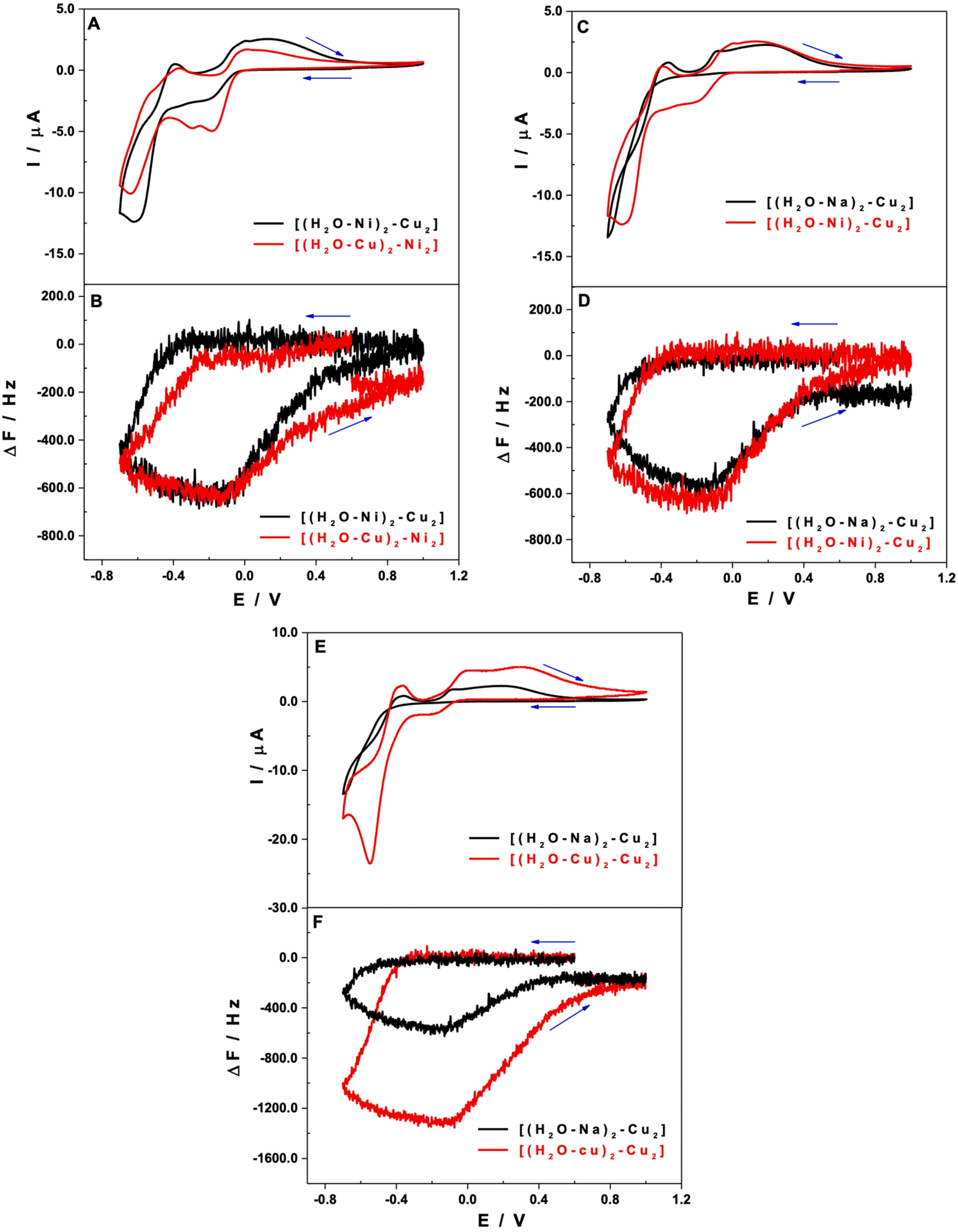

Fig. 10. CVs recorded on a GC-coated quartz crystal electrode at 5 mV s^{-1} in pH 4.0 electrolyte (0.4 M CH_3COOLi + CH_3COOH). (A-B) **$[(H_2O\text{-}Ni)_2\text{-}Cu_2]$** (black) and **$[(H_2O\text{-}Cu)_2\text{-}Ni_2]$** (red): (A) CVs; (B) vibration frequency variation as a function of potential. Scans extended to the first reduction step of W(VI) centres. (C-D) **$[(H_2O\text{-}Na)_2\text{-}Cu_2]$** (black) and **$[(H_2O\text{-}Ni)_2\text{-}Cu_2]$**: (C) CVs; (D) vibration frequency variation versus potential. Scans extended to the first reduction step of W(VI) centres. (E–F) **$[(H_2O\text{-}Na)_2\text{-}Cu_2]$** (black) and **$[(H_2O\text{-}Cu)_2\text{-}Cu_2]$** (red): (E) CVs; vibration frequency variation versus potential. Scans extended to the first reduction step of W (VI) centres.

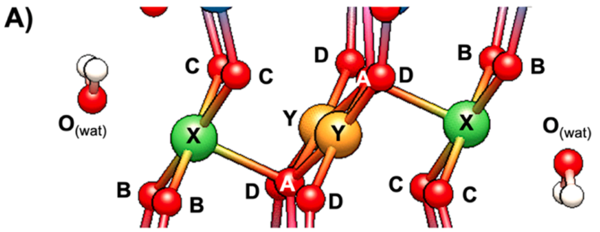

B)

Bond	X = Ni, Y = Cu	X = Na, Y = Ni	X = Na, Y = Cu
X-$O_{(wat)}$	2.211	2.465	2.540
X-A	2.089	2.569	2.557
X-B	2.012	2.207	2.166
X-C	2.106	2.435	2.337
Y-D	1.982	2.070	2.035
Y-A	2.017	2.041	1.997
Y-C	2.235	2.068	2.247

Fig. 11. A) Schematic representation of the equatorial region, illustrating the coordination environment of external (X) and internal (Y) metal centers with oxygen atoms (A-D and $O_{(wat)}$, red spheres). B) Bond lengths (in Å) for the 12-fold protonated **$[(H_2O\text{-}Ni)_2\text{-}Cu_2]$** and 14-fold protonated **$[(H_2O\text{-}Na)_2\text{-}Ni_2]$** / **$[(H_2O\text{-}Na)_2\text{-}Cu_2]$** systems, highlighting structural variations upon protonation and metal substitution.

reported for Fe^{2+} (2.23 Å)[67] and Co^{2+} (2.24 Å) [68] In contrast, for **$[(H_2O\text{-}Cu)_2\text{-}Cu_2]$**, the computed Cu–$O_{(wat)}$ bond distance is 2.34 Å, thus 0.12 Å longer than the Ni–$O_{(wat)}$ bonds. This is inherent to the d^9 electronic configuration of Cu^{2+}, in combination with associated Jahn-–Teller distortions. In Fig. 11, the Jahn-Teller distortion can be noticed in the protonated system of **$[(H_2O\text{-}Ni)_2\text{-}Cu_2]$**, where two bonds between Cu and O are ~0.22–0.25 Å longer than the other four. These facts highlight the sensitive connection between the local metal geometry and its electronic configuration.

In mixed-metal systems, with Cu and Ni, the optimised geometries show subtle variations in bond lengths, reflecting the interplay between the different metal centers. The external metal sites, often occupied by Cu atoms, exhibit slightly different coordination environments compared to the internal sites. Notably, the X–$O_{(wat)}$ distances (Table S3) are markedly labile, adjusting dynamically during the optimisation process to maximise overall stabilisation. This dynamic behaviour accounts for the adaptability of the POM structure, which can accommodate diverse metals and coordination modes without compromising its overall integrity. For the system **$[(Na\text{-}OH_2)_2\text{-}Ni_2]$** and its 14-fold protonated form $[(Na\text{-}OH_2)_2\text{-}Ni_2H_{14}]^{4-}$, the computed bond lengths correlate well with experimental X-ray crystallography data, albeit with slight deviations. For example, the Na–$O_{(wat)}$ bond distances are observed to be marginally shorter from crystal structure determination [52], a discrepancy attributed to differences between solvent-phase and crystal-phase environments.

We performed a molecular dynamics simulation to reveal the behaviour of the water units attached to the external equatorial metals (X). Details of the calculation can be found in the ESI. From the resulting trajectory we can observe that the external Ni atoms retain a water molecule coordinated each along the entire simulation, with an average Ni−$O_{(wat)}$ distance of 1.94 Å (Figure S23), further supporting the experimentally reported behaviour of these systems. Moreover, not only do the water molecules coordinated to the metal remain fixed, but also do other H_2O molecules also located around the equatorial region of the POM sandwich, forming hydrogen bonds with accessible oxo groups of the POM. Thus, more near-to-metal water molecules are available in the catalytic region.

4.2. Electronic structure and protonation

We herein aim to correlate the composition and arrangement of the atoms in the equatorial region with the electron distribution and, ultimately, the calculated and experimental redox properties are compared. Another relevant feature is the electronic structure related on the W-based regions. These two $As_2W_{15}O_{56}$ hemispheres of the sandwich POMs present the typical sequence of delocalised molecular orbitals, where the highest occupied and the lowest unoccupied orbitals (HOMO and LUMO) are combinations of p-oxygen and d-tungsten orbitals, respectively (see Figure S24 for the results on the $[As_2W_{15}O_{56}]^{12-}$ precursor) [69] Furthermore, the equatorial region composed of Cu or/and Ni centers in sandwich structures can lead to new features in the orbital scheme, notably changing what the HOMO and LUMO become in terms of spatial distribution, energy and mutual gap [70] Namely, how the electronic properties and part of the reactivity are modulated.

Fig. 12, in combination with Figure S25, help us to discern the systems with LUMOs associated with the **As_2W_{15}** regions. Of course, this fact depending on the metal composition of the equatorial region. Except for **$[(Na\text{-}OH_2)_2\text{-}Ni_2]$**, with a charge of −18 (Fig. 12A), the rest of the HOMO energies are practically identical, as expected for their equal molecular charge. By contrast, the LUMOs notably depend on the equatorial composition (see also Fig. 12B). For example, remarkable is the difference between the LUMO energy of −2.73 eV for **$[(Ni\text{-}OH_2)_2\text{-}Ni_2]$** and those ranging from −3.0 to −3.2 eV upon incorporation of Cu (II). These more accessible empty orbitals justify the appearance of Cu reduction waves at lower potentials in the latter cases. The spatial distribution of these frontier molecular orbitals informs about the preferred location of the extra electrons upon reduction. Figure S25A-C represents the α and β HOMOs and LUMOs for the fully oxidised systems. In Figure S25A, both LUMO components are dominated by W contributions, confirming that the **As_2W_{15}** redox fingerprint is maintained in Cu-free systems, **$[(Na\text{-}OH_2)_2\text{-}Ni_2]$** and **$[(Ni\text{-}OH_2)_2\text{-}Ni_2]$**. Figure S25B, by contrast, shows Cu-centered β-LUMOs in **$[(Na\text{-}OH_2)_2\text{-}Cu_2]$** and **$[(Cu\text{-}OH_2)_2\text{-}Cu_2]$**, a proof that the first reduction wave is Cu(II) + e → Cu(I). The two mixed-metal Ni/Cu systems (Figure S25C) also present Cu-centered β-LUMOs, in accordance with CV evidence. At this point, the origin of the highest reduction intensity measured for the **$[(Cu\text{-}OH_2)_2\text{-}Cu_2]$** compared to those of mixed-metal systems, is not clear. The computational approaches used in the present work do not inform on (complex) kinetic aspects. However, we briefly take up this point below.

The degree of protonation of POMs in solution is a relevant, though elusive, topic. Because the bare systems carry high negative charges (−16 or −18), protonation is expected to be significant even in mild acidic conditions. Therefore, additional calculations were performed on the following models: 8- and 12-fold protonated for Cu/Ni systems, and 10- and 14-fold protonated for Na-containing systems. Based on these results, we explored the changes in the electronic and redox properties of the complexes. To identify the favourable sites for proton attachment, taking the computed total electron densities of the unprotonated systems, we mapped the directly related electrostatic potential function (ESP). In Figure S26A, the locations at which incoming protons are more attracted for can be identified, namely, the equatorial oxygens and some nearby positions in the $W_{15}O_{56}$ framework (Figure S26B). In the absence of a direct and precise experimental quantification of the number of protons in the system at a given pH, this relevant parameter was guessed by comparing the LUMO energies of the present and other well-characterised species [69] Approximately, the LUMO orbitals of fully oxidised classical POMs are found between −3.5 and −4.5 eV at this level of calculation.

The electronic structures of the most highly protonated systems calculated are shown in Figure S27, with a molecular charge of −4 after addition of 12 and 14 protons to Ni/Cu-only and Na-containing systems, respectively. The molecular orbital diagrams of the three protonated

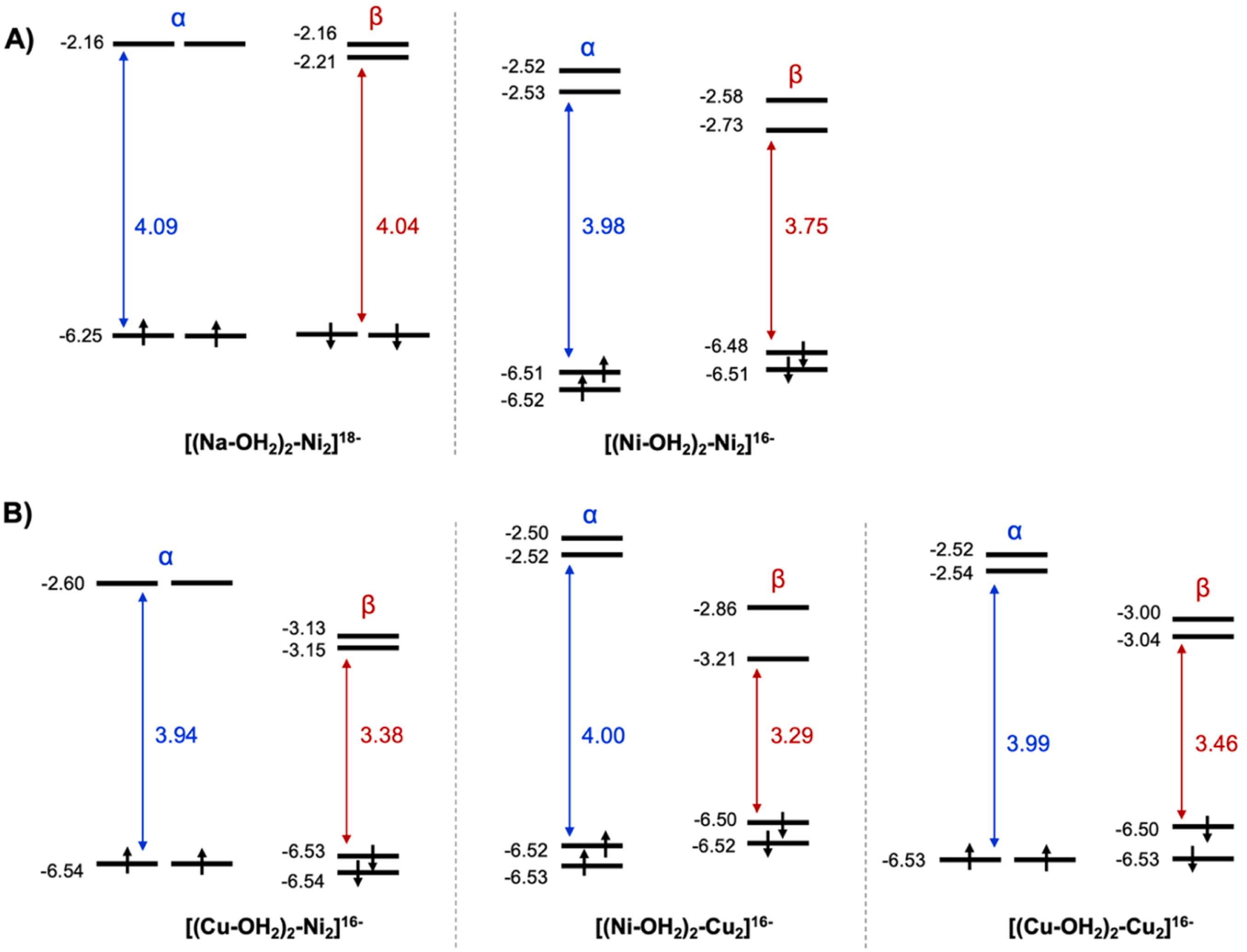

Fig. 12. Molecular orbital diagram (values in eV, not to scale) for non-protonated systems, with electrons represented as arrows. The α and β orbital sets are shown with the highest occupied and lowest unoccupied orbitals of each set, along with their energy gaps. Except for the system represented with charge −18, the rest feature the same energies in the highest occupied orbitals. A) Cu-free POMs, B) Cu-containing POMs.

systems reveal some differences, especially in the β-spin set, with energy gaps systematically lower in Cu-containing systems stemming from the d^9 electronic configuration of Cu^{2+}, which makes it more susceptible to accepting electrons. Comparing the LUMOs of **$[(H_2O\text{-}Ni)_2\text{-}Cu_2H_{12}]^{4-}$** and **$[(H_2O\text{-}Na)_2\text{-}Cu_2H_{14}]^{4-}$** one can see that the former is lower in energy (−4.48 eV), a fact that reinforces the idea of a synergistic effect if Ni is combined with Cu, facilitating the first Cu reduction if compared to Na/Cu systems. This interplay between orbital availability and electronic reactivity underlines the role of each metal center in the equatorial region in modulating the redox properties in these systems.

4.3. Redox properties

To support the redox measurements discussed above, DFT calculations were performed by the addition of electrons based on the reaction POM + ne^- → POM^{n-}. The Gibbs free energy change (ΔG_{red}) associated with this process is related to the reduction potential (indicated as V_{red} in this section) by $\Delta G_{red} = -nFV_{red}$, where n is the number of electrons transferred and F = 96,485 C mol^{-1} is Faraday's constant. Computationally, the electronic energy difference between the oxidised (POM) and the reduced (POM^{n-}) states, or reduction energy, is E_{red}. Under the assumption that the entropy change (ΔS) of such electron exchange processes is small, it is reasonable to assume $E_{red} \approx \Delta G_{red}$, allowing us to directly relate the computed E_{red} with the reduction potentials, V_{red}. For a fair comparison, both the computed (E_{red}) and the experimental (V_{red}) values must be referred to the same reference electrode potential. Since our experiments were conducted using the SCE, with an absolute reduction energy of −4.68 eV [71], the computed reduction potentials (E_{red}') were obtained by combining this value with the calculated E_{red}. The same methodological framework used for unprotonated systems was then applied to compute the reduction potentials of the protonated species, allowing us to assess the influence of protonation on the redox behavior.

The dependency of the frontier orbital energies, including HOMO and LUMO) is connected to the redox behaviour. Protonation leads to substantial changes in the HOMO and LUMO energies and, thus, in the ability of the POM to accept or donate electrons. Consequently, the differences computed for HOMO and LUMO energies of **$[(H_2O\text{-}Ni)_2\text{-}Ni_2]$**, **$[(H_2O\text{-}Na)_2\text{-}Ni_2]$** and Cu-containing systems can explain the more favourable reduction of the latter in cyclic voltammetry studies. In Figure S28, the frontier molecular orbital energies vs the protons added are represented for **$[(H_2O\text{-}Ni)_2\text{-}Cu_2]$** as an example. The LUMO (a β orbital belonging to Cu) is 0.53 eV and 1.27 eV lower in the 8- and 12-protonated forms than in the unprotonated one, respectively, suggesting considerable voltage changes in the reduction waves.

The following shifts in reduction potentials were calculated. The unprotonated species has E_{red}' = −1.485 V vs. SCE, whereas the 8-protonated form (charge −8) has E_{red}' = −0.903 V (a positive shift of

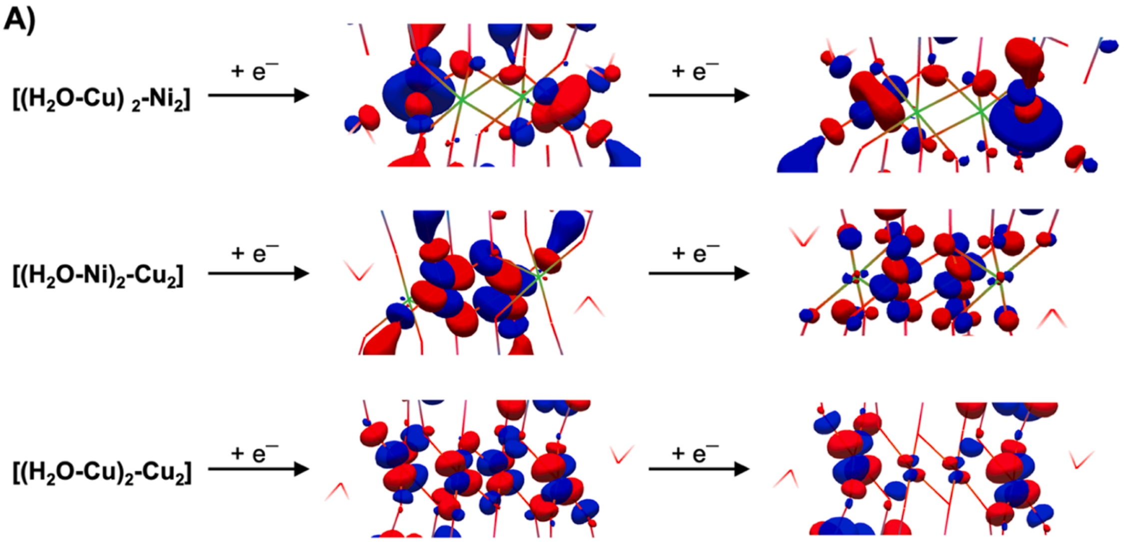

B)

System	X	Y
$[(Cu\text{-}OH_2)_2\text{-}Cu_2]^{16-}$	0.736	0.732
$[(Cu\text{-}OH_2)_2\text{-}Cu_2\ 1e]^{17-}$	0.596	0.667
$[(Cu\text{-}OH_2)_2\text{-}Cu_2\ 2e]^{18-}$	0.379	0.729

Fig. 13. A) Representations, focused on the equatorial region as shown in Fig. 11A, of the molecular orbitals accepting the first two extra β electrons three different POM systems. Cu are the accepting centres in all cases. B) Atomic spin densities in external (X) and internal (Y) Cu atoms in fully oxidised, and one- and two-electron reduced forms **$[(H_2O\text{-}Cu)_2\text{-}Cu_2]$**.

0.582 V), and the 12-protonated form (charge −4) presents E_{red}' = –0.086 V, and an accumulated E_{red}' shift of 1.40 V relative to the unprotonated species. These values are consistent both with the frontier orbital energy variations and the CV data, proving at the molecular scale how much protonation affects the redox properties in sandwich-type POMs.

These computational results reliably capture the reduction of Cu^{2+} centres within the POM framework, but only from Cu(II) to Cu(I). Attempts to tackle theoretically further reduction to Cu(0) were not fruitful, remaining an open theoretical aspect that involves complex interfacial phenomena, i.e., deposition of copper atoms on the electrode surface and, probably, arrangement into a (partially) ordered Cu lattice.

Analysis of the Mulliken atomic spin density (ASD) helps elucidating other aspects of the transition metal centers. In fully oxidised sandwich POMs, unpaired electrons are localised in the equatorial region. Table S4 in the ESI lists the metal and oxygen centers, labeled as in Fig. 11A, their corresponding abundance, and their ASD for the systems discussed. The total α spin population follows a trend reflecting the electronic configurations of Ni^{2+} (d^8, two unpaired electrons) and Cu^{2+} (d^9, one unpaired electron). The spin density is primarily localised on the metal centers X and Y, with Ni-rich systems exhibiting the highest values. By contrast, the oxygen atoms $O_{(wat)}$, A, B, C, and D display much lower spin densities, suggesting limited delocalisation of unpaired electrons onto the ligand framework. The number of unpaired electrons decreases from 8 in the **$[(H_2O\text{-}Ni)_2\text{-}Ni_2]$** system to 6 in **$[(H_2O\text{-}Ni)_2\text{-}Cu_2]$** and **$[(H_2O\text{-}Cu)_2\text{-}Ni_2]$**, 4 in **$[(H_2O\text{-}Cu)_2\text{-}Cu_2]$** and **$[(H_2O\text{-}Na)_2\text{-}Ni_2]$**, and 2 in **$[(H_2O\text{-}Na)_2\text{-}Cu_2]$**. If we focus on Ni centers, the ASD lies in a narrow range of 1.734–1753, and for Cu centers 0.664–0.743. The small 0.664 value for Cu in the **$[(H_2O\text{-}Na)_2\text{-}Cu_2]$** system is compensated by a large ASD for O_A (0.150) directly bonded to them. Thus, in mixed-metal systems there is some spin density redistribution, with external Cu atoms emerging as critical sites for initial electron uptake in reduction processes.

For Ni/Cu POMs, the first and second extra electrons are clearly localised on the two Cu atoms, which become Cu(I), despite their position (first two lines in Fig. 13A). Turning to **$[(H_2O\text{-}Cu)_2\text{-}Cu_2]$**, the first extra electron gets delocalised over the four Cu centers, as reflected in the accepting molecular orbital (third row). This is illustrated with the uniform ASD distribution among these sites, which change from 0.736 to 0.596 in external positions and from 0.732 to 0.667 in internal positions (values in Fig. 13B). This delocalisation helps to stabilise the initial reduced state and is consistent with the lower potential and higher intensity for this reduction wave. For the second extra electron, the molecular orbital suggests a significant localisation on external Cu sites (third row), confirmed by ASD values for the 2e-reduced **$[(H_2O\text{-}Cu)_2\text{-}Cu_2]$**, with spin density on X = 0.379 and Y = 0.729 (the latter equal to the original fully oxidised situation). These facts illustrate the stepwise electron transfer processes that are observed in CV experiments from a molecular orbital perspective.

4. Conclusions

Experimental characterizations, relying on techniques such as XPS and various electrochemical methods, played a crucial role in elucidating the electrochemical behavior of the compounds presented. These allowed us to unequivocally establish the chemical composition and structure of the novel copper and nickel mixed-sandwich POMs. These results were confirmed by rigorous comparison with their monometallic counterparts, i.e., previously described sandwich POMs containing either only copper or only nickel. Electrochemistry measurements allowed us to define redox features of the various compounds analysed. In particular, the electrode deposition of Cu(0) in the cathodic regime and redissolution in the anodic regime. The absence of waves in POMs based on Na and/or Ni distinctive of the W-only system establishes that, in these cases, the equatorial region does not significantly modify the fingerprint of the precursor polyoxotungstate.

We have integrated computational chemistry results into these experimental findings. The geometries derived from DFT optimisations highlight the influence of the metal identity and coordination on specific structural features. First-order Jahn-Teller distortions were identified in the coordination spheres of Cu(II) atoms, at variance with Ni(II) centers in the present systems. The study clarifies how the tungsten–oxygen framework establishes the fundamental electronic scaffold, while the localised effects introduced by transition metal centers, together with protonation, modulate the redox behaviour. For the electronic features, the nature and energy of the molecular orbitals involved in reduction processes support, or confirm, the redox properties of these new sandwich-type POMs. The differential role of Cu(II) centers is underpinned as their LUMO energies and shapes reveal. Calculations illustrate that Na/Ni and Ni-only POMs have W-based LUMOs, thus their electrochemical fingerprints are those of As_2W_{15} with only minor peak potential differences. The degree of protonation, although not certainly known with the present techniques, has been discussed for one of the systems to emphasise its relevance on the electrochemical measurements. Namely, we tracked the calculated LUMO energy and the reduction energy with respect to the number of protons. Also important is to assess and compare the redox fingerprints of W-only POMs and Ni/Cu-containing systems. Although our present computational approach cannot capture the dynamic processes associated with copper deposition on electrodes, the insights obtained from our calculations help to understand the main redox features of sandwich POMs.

Notes

The authors declare no competing interests.

Supporting Information: The following files are available free of charge: additional characterisation data and analysis (PDF).

CRediT authorship contribution statement

Anaïs Abrousse: Formal analysis, Investigation, Methodology, Writing – original draft, Writing – review & editing. **Ionut-Octavian Stan:** Data curation, Formal analysis, Investigation, Methodology, Visualization, Writing – original draft, Writing – review & editing. **Neus Vilà:** Conceptualization, Data curation, Formal analysis, Investigation, Methodology, Supervision, Validation, Visualization, Writing – original draft, Writing – review & editing. **Anne-Lucie Teillout:** Formal analysis, Methodology, Validation, Visualization, Writing – review & editing. **Khaoula Merimi:** Formal analysis, Investigation, Methodology, Visualization, Writing – review & editing. **Coen de Graaf:** Conceptualization, Formal analysis, Funding acquisition, Investigation, Methodology, Project administration, Resources, Software, Supervision, Validation, Visualization, Writing – review & editing. **Pedro de Oliveira:** Formal analysis, Methodology, Validation, Visualization, Writing – review & editing. **Xavier López:** Conceptualization, Formal analysis, Investigation, Methodology, Project administration, Resources, Software, Supervision, Validation, Visualization, Writing – original draft, Writing – review & editing. **Israël Martyr Mbomekallé:** Conceptualization, Data curation, Formal analysis, Funding acquisition, Investigation, Methodology, Project administration, Resources, Supervision, Validation, Visualization, Writing – original draft, Writing – review & editing.

Declaration of competing interest

The authors declare that they have no known competing financial interests or personal relationships that could have appeared to influence the work reported in this paper.

Acknowledgments

A.A., A.-L.T., P.d.O. and I.M.M. thank the CNRS, the Université Paris-Saclay for financial support and the ADI 2022 project funded by the IDEX Paris-Saclay, ANR-11-IDEX-0003–02 ANR-11-IDEX-0003–02.

X.L, C.d.G., K.M. and I.-O.S. thank support from the Generalitat de Catalunya [project 2021SGR00110] and from the Spanish Government [grant PID2023–149905NB-I00, funded by MCINAEI/ 10.13039/501100011033].

N.V. thanks the spectroscopy and microscopy Service Facility (SMI) of the LCPME for providing access to the XPS apparatus.

Supplementary materials

Supplementary material associated with this article can be found, in the online version, at doi:10.1016/j.electacta.2025.147858.

Data availability

Data will be made available on request.

References

[1] R. Contant, G. Herve, The heteropolyoxotungstates: relationships between routes of formation and structures, Rev. Inorg. Chem. (2002) 63.
[2] Polyoxometalates, Update Based On the Original Article By Michael T. Pope, Encyclopedia of Inorganic Chemistry ©, John Wiley & Sons, Ltd, in Encyclopedia of Inorganic and Bioinorganic Chemistry, 2005.
[3] D.E. Katsoulis, A survey of applications of polyoxometalates, Chem. Rev. 98 (1) (1998) 359–388.
[4] A. Müller, et al., Polyoxometalates: very large ClustersNanoscale magnets, Chem. Rev. 98 (1) (1998) 239–272.
[5] M. Sadakane, E. Steckhan, Electrochemical properties of polyoxometalates as electrocatalysts, Chem. Rev. 98 (1) (1998) 219–238.
[6] A. Müller, P. Kögerler, From simple building blocks to structures with increasing size and complexity, Coord. Chem. Rev. 182 (1) (1999) 3–17.
[7] E. Coronado, C. Giménez-Saiz, C.J. Gómez-García, Recent advances in polyoxometalate-containing molecular conductors, Coord. Chem. Rev. 249 (17) (2005) 1776–1796.
[8] D.-L. Long, R. Tsunashima, L. Cronin, Polyoxometalates: building blocks for functional nanoscale systems, Angew. Chem. Int. Ed. 49 (10) (2010) 1736–1758.
[9] J.J. Walsh, et al., Hybrid polyoxometalate materials for photo(electro-) chemical applications, Coord. Chem. Rev. 306 (2016) 217–234.
[10] M.T. Pope, A. Müller, Polyoxometalate chemistry: an old field with new dimensions in several disciplines, Angew. Chem. Int. Ed. Engl. 30 (1) (1991) 34–48.
[11] N.I. Gumerova, A. Rompel, Synthesis, structures and applications of electron-rich polyoxometalates, Nat. Rev. Chem. 2 (2018) 0112.
[12] T. Ueda, Electrochemistry of polyoxometalates: from fundamental aspects to applications, ChemElectroChem 5 (6) (2018) 823–838.
[13] M.T. Pope, G.M. Varga, Heteropoly blues. I. Reduction stoichiometries and reduction potentials of some 12-tungstates, Inorg. Chem. 5 (7) (1966) 1249–1254.
[14] M.T. Pope, E. Papaconstantinou, Heteropoly blues. II. Reduction of 2:18-tungstates, Inorg. Chem. 6 (6) (1967) 1147–1152.
[15] M.T. Pope, Heteropoly and isopoly anions as oxo complexes and their reducibility to mixed-valence blues, Inorg. Chem. 11 (8) (1972) 1973–1974.
[16] B. Keita, L. Nadjo, Electrochemistry of isopoly and heteropoly oxometalates, Encycl. Electrochem. (2007).
[17] B. Keita, T. Lucas, L. Nadjo, New aspects of the electrochemistry of heteropoly acids. Reduction currents as a probe of solvent-electrolyte interactions, J. Electroanal. Chem. Interfacial Electrochem. 208 (2) (1986) 343–356.
[18] B. Keita, L. Nadjo, New aspects of the electrochemistry of heteropolyacids. Part IV. Acidity dependent cyclic voltammetric behavior of phosphotungstic and silicotungstic heteropolyanions in water and N,N-dimethylformamide, J. Electroanal. Chem. Interfacial Electrochem. 227 (1–2) (1987) 77–98.
[19] B. Keita, L. Nadjo, Heterogeneous one-electron exchange of silicotungstic heteropolyanion in dimethylformamide, J. Electroanal, Chem. Interfacial Electrochem. 219 (1–2) (1987) 355–363.
[20] B. Keita, L. Nadjo, New aspects of the electrochemistry of heteropolyacids. Part II. Coupled electron and proton transfers in the reduction of silicotungstic species, J. Electroanal. Chem. Interfacial Electrochem. 217 (2) (1987) 287–304.
[21] B. Keita, A. Mahmoud, L. Nadjo, EQCM monitoring of charge transport processes in polyaniline films doped with 12-silicomolybdic heteropolyanion, J. Electroanal. Chem. 386 (1–2) (1995) 245–251.
[22] B. Keita, et al., Electrochemical quartz crystal microbalance: evidence for the adsorption of heteropoly and isopoly anions on gold electrodes, J. Electroanal. Chem. 384 (1–2) (1995) 155–169.
[23] E. Abdeljalil, et al., STM and AFM characterization of thin metal oxide films electrodeposited from [P2Mo18O62]6, J. Solid. State Electrochem. 5 (2) (2001) 94–106.
[24] B. Keita, et al., Toward a qualitative understanding of the initial electron transfer site in Dawson-type heteropolyanions, New. J. Chem. 26 (10) (2002) 1314–1319.
[25] S. Romo, et al., Density functional theory and ab initio study of electronic and electrochemistry properties of the Tetranuclear Sandwich Complex [FeIII4(H2O)2(PW9O34)2]6, Inorg. Chem. 46 (10) (2007) 4022–4027.

[26] I.M. Mbomekalle, et al., Lacunary Wells-Dawson sandwich complexes - synthesis, characterization, and stability studies of multi-iron species, Eur. J. Inorg. Chem. (21) (2003) 3924–3928.

[27] I.M. Mbomekalle, et al., Synthesis, structural characterization, and electrocatalytic studies of αββα-(ZnIIOH2)2(FeIII)2(X2W15O56)214- (X = P or As), C. R. Chim. 8 (6–7) (2005) 1077–1086.

[28] I.M. Mbomekalle, et al., Rational synthesis, structure, magnetism and electrochemistry of mixed iron-nickel-containing Wells-Dawson-fragment-based sandwich-type polyoxometalates, Eur. J. Inorg. Chem. (34) (2009) 5194–5204.

[29] F. Doungmene, et al., Electrochemical behavior of mixed d metal-iron containing Wells-Dawson sandwich-type complexes: [(FeOH2)2M2(X2W15O56)2]n- and [(MOH2)2Fe2(X2W15O56)2]n- (M = CrIII, MnIII, MnII, CoII, NiII, CuII, ZnII, X = AsV or PV and n = 12 or 14), Electrochim. Acta 125 (2014) 674–682.

[30] C.S. Ayingone Mezui, et al., Synthesis, structure, and magnetic electrochemical properties of a Family of tungstoarsenates containing just CoII centers or both CoII and FeIII centers, Inorg. Chem. 56 (4) (2017) 1999–2012.

[31] F. Doungmene, et al., Synthesis, electrochemistry and electro-catalytic properties of the mixed copper-iron-containing sandwich-type polyoxometalates [(FeIIIOH)2CuII 2 (X2W15O56)2]14- and [(CuIIOH2)2FeIII 2(X2W15O56)2]14- (with X = AsV and PV), Curr. Inorg. Chem. 7 (1) (2017) 28–38.

[32] D. Jabbour, et al., Investigation of multi-nickel-substituted tungstophosphates and their stability and electrocatalytic properties in aqueous media, Eur. J. Inorg. Chem. (10) (2004) 2036–2044.

[33] B.S. Bassil, et al., Heptanickel(II) double-cubane core in Wells-Dawson heteropolytungstate, [Ni7(OH)6(H2O)6(P2W15O56)2]16, Chem. Commun. 52 (12) (2016) 2601–2604.

[34] B. Keita, L. Nadjo, Polyoxometalate-based homogeneous catalysis of electrode reactions: recent achievements, J. Mol. Catal. A: Chem. 262 (1–2) (2007) 190–215.

[35] B. Keita, et al., [H4AsW18O62]7-, a novel Dawson heteropolyanion and two of its sandwich-type derivatives [Zn4(H2O)2(H4AsW15O56)2]18-, [Cu4(H2O)2(H4AsW15O56)2]18-: cyclic voltammetry and electrocatalytic properties towards nitrite and nitrate, Electrochem. Commun. 3 (6) (2001) 267–273.

[36] B. Keita, I.-M. Mbomekalle, L. Nadjo, Redox behaviors and electrocatalytic properties of copper within Dawson structure-derived sandwich heteropolyanions [Cu4(H2O)2(X2W15O56)2]16- (X=P or As), Electrochem. Commun. 5 (9) (2003) 830–837.

[37] I.M. Mbomekalle, et al., Electrocatalytic reduction of O2 by a Cu(II)-substituted electron-rich wheel-type oxomolybdate nanocluster, J. Clust. Sci. 17 (2) (2006) 333–348.

[38] B. Keita, et al., Dioxygen and hydrogen peroxide electrocatalytic reduction: evidence for a cooperativity of Mo and Cu centers in substituted heteropolyanions, Electrochem. Commun. 4 (8) (2002) 663–668.

[39] B. Keita, et al., Cyclic voltammetric evidence of facilitation of the reduction of nitrite by the presence of molybdenum in Fe- or Cu-substituted heteropolytungstates, J. Electroanal. Chem. 508 (1–2) (2001) 70–80.

[40] B. Keita, et al., Cooperativity of copper and molybdenum centers in polyoxometalate-based electrocatalysts: cyclic voltammetry, EQCM, and AFM characterization, Langmuir 22 (25) (2006) 10416–10425.

[41] S. Imar, et al., Enhancement of nitrite and nitrate electrocatalytic reduction through the employment of self-assembled layers of nickel- and copper-substituted crown-type heteropolyanions, Langmuir 31 (8) (2015) 2584–2592.

[42] L.H. Bi, et al., Synthesis, characterization and crystal structure of a novel 2D network structure based on hexacopper(II) substituted tungstoantimonate, Inorg. Chim Acta 362 (9) (2009) 3309–3313.

[43] Z.M. Zhang, et al., Two multi-copper-containing heteropolyoxotungstates constructed from the lacunary keggin polyoxoanion and the high-nuclear spin cluster, Inorg. Chem. 46 (20) (2007) 8162–8169.

[44] D. Jabbour, et al., The wheel-shaped Cu20-tungstophosphate Cu20Cl(H)24(H2O)12(P8W48O184) 25-, redox and electrocatalytic properties, Electrochem. Commun. 7 (8) (2005) 841–847.

[45] H. El Moll, et al., Properties of a tunable multinuclear nickel polyoxotungstate platform, Chem.-Eur. J. 19 (21) (2013) 6753–6765.

[46] D.V. Jawale, et al., Carbon nanotube-polyoxometalate nanohybrids as efficient electro-catalysts for the hydrogen evolution reaction, Carbon. N. Y. 188 (2022) 523–532.

[47] B.S. Bassil, et al., 15-Copper(ii)-containing 36-tungsto-4-silicates(iv) Cu15O2(OH)10X(A–SiW9O34)4 25- (X = Cl, Br): synthesis, structure, magnetic properties, and electrocatalytic CO2 reduction, Dalton. Trans. 47 (35) (2018) 12439–12448.

[48] R. Belghiche, et al., Synthesis and characterization of Fe- or Cu-substituted molybdenum-enriched tungstodiphosphates, Eur. J. Inorg. Chem. (6) (2002) 1410–1414.

[49] I.M. Mbomekalle, et al., Rationalization and improvement of the syntheses of two octadecatungstoarsenates: the novel α-K7[H4AsW18O62]·18H2O and the well known symmetrical α-K6[As2W18O62]·14H2O, Inorg. Chim Acta 342 (2003) 219–228.

[50] R. Contant, R. Thouvenot, Hétéropolyanions de type Dawson. 2. Synthèses de polyoxotungstoarsénates lacunaires dérivant de l`octadécatungstodiarsénate. Étude structurale par RMN du tungstène-183 des octadéca (molybdotungstovanado)diarsénates apparentés, Can. J. Chem. 69 (10) (1991) 1498–1506.

[51] T.M. Anderson, et al., Structural and electrochemical studies of dicupric Wells-Dawson sandwich-type complexes, J. Clust. Sci. 17 (2) (2006) 183–195.

[52] I.M. Mbomekalle, et al., Rational synthesis, structure, magnetism and electrochemistry of mixed iron–Nickel-containing wells–Dawson-fragment-based sandwich-type polyoxometalates, Eur. J. Inorg. Chem. 2009 (34) (2009) 5194–5204.

[53] A.-L. Teillout, et al., Synthesis, crystal structure, electrochemistry and electro-catalytic properties of the Manganese-containing polyoxotungstate, [(Mn(H2O)3)2(H2W12O42)]6−, Inorganics 7 (2) (2019) 15.

[54] M.J. Frisch, G.W.T., H.B. Schlegel, G.E. Scuseria, M.A. Robb, J.R. Cheeseman, G. Scalmani, Gaussian 16, Revision B.0, V. Barone, G. A. Petersson, H. Nakatsuji, X. Li, M. Caricato, A. V. Marenich, J. Bloino, B. G. Janesko, R. Gomperts, B. Mennucci, H. P. Hratchian, J. V. Ortiz, A. F. Izmaylov, J. L. Sonnenberg, D. Williams-Young, F. Ding, F. Lipparini, F. Egidi, J. Goings, B. Peng, A. Petrone, T. Henderson, D. Ranasinghe, V. G. Zakrzewski, J. Gao, N. Rega, G. Zheng, W. Liang, M. Hada,M. Ehara, K. Toyota, R. Fukuda, J. Hasegawa, M. Ishida, T. Nakajima, Y. Honda, O. Kitao, H. Nakai, T. Vreven, K. Throssell, J. A. Montgomery, Jr., J. E. Peralta, F. Ogliaro, M. J. Bearpark, J. J. Heyd, E. N. Brothers, K. N. Kudin, V. N. Staroverov, T. A. Keith, R. Kobayashi, J. Normand, K. Raghavachari, A. P. Rendell, J. C. Burant, S. S. Iyengar, J. Tomasi, M. Cossi, J. M. Millam, M. Klene, C. Adamo, R. Cammi, J. W. Ochterski, R. L. Martin, K. Morokuma, O. Farkas, J. B. Foresman, and D. J. Fox, Gaussian Inc, Wallingford CT, 2016.

[55] G. te Velde, et al., Chemistry with ADF, J. Comput. Chem. 22 (9) (2001) 931–967.

[56] A.D. Becke, Density-functional exchange-energy approximation with correct asymptotic behavior, Phys. Rev. a 38 (6) (1988) 3098–3100.

[57] E. van Lenthe, A. Ehlers, E.-J. Baerends, Geometry optimizations in the zero order regular approximation for relativistic effects, J. Chem. Phys. 110 (18) (1999) 8943–8953.

[58] C.C. Pye, T. Ziegler, An implementation of the conductor-like screening model of solvation within the Amsterdam density functional package, Theor. Chem. Acc. 101 (6) (1999) 396–408.

[59] A.D. Becke, Density-functional thermochemistry. III. The role of exact exchange, J. Chem. Phys. 98 (7) (1993) 5648–5652.

[60] P.J. Stephens, et al., Ab initio calculation of vibrational absorption and circular dichroism spectra using density functional force fields, J. Phys. Chem. 98 (45) (1994) 11623–11627.

[61] S. Miertuš, E. Scrocco, J. Tomasi, Electrostatic interaction of a solute with a continuum. A direct utilizaion of AB initio molecular potentials for the prevision of solvent effects, Chem. Phys. 55 (1) (1981) 117–129.

[62] S. Grimme, Accurate description of van der Waals complexes by density functional theory including empirical corrections, J. Comput. Chem. 25 (12) (2004) 1463–1473.

[63] L. Martin, et al., Comprehensive X-ray photoelectron spectroscopy study of the conversion reaction mechanism of CuO in lithiated thin film electrodes, J. Phys. Chem. C 117 (9) (2013) 4421–4430.

[64] D. Jabbour, et al., The wheel-shaped Cu20-tungstophosphate [Cu20Cl(OH)24(H2O)12(P8W48O184)]25-, redox and electrocatalytic properties, Electrochem. Commun. 7 (8) (2005) 841–847.

[65] B. Keita, et al., Salient electrochemical and electrocatalytic behaviour of the crown heteropolyanion K28Li5H7P8W48O184·92H2O, Electrochem. commun. 2 (10) (2000) 720–726.

[66] B. Keita, L. Nadjo, et al., Electrochemistry of Isopoly and Heteropoly oxometalates, in Encyclopedia of Electrochemistry, Bard, 7, Wiley-VCH, 2005. Editors.

[67] K. Azmani, Efficient catalysts for water oxidation: synthesis, characterization and computational study. Departament De Química Física i Inorgànica, Universitat Rovira i Virgili, 2022, p. 180.

[68] J. Soriano-López, et al., Tetracobalt-polyoxometalate catalysts for water oxidation: key mechanistic details, J. Catal. 350 (2017) 56–63.

[69] X. López, et al., Structure, properties and reactivity of polyoxometalates: a theoretical perspective, Chem. Soc. Rev. 41 (22) (2012) 7537–7571.

[70] HOMO: highest occupied molecular orbital; LUMO: lowest unoccupied molecular orbital.

[71] S. Trasatti, The absolute electrode potential: an explanatory note (Recommendations 1986), Pure Appl. Chem. 58 (7) (1986) 955–966.